

Intensification and Northward Extension of Northwest Pacific Anomalous Anticyclone in El Niño Decaying Mid-Summer: An Energetic Perspective

Haosu Tang

Institute of Atmospheric Physics Chinese Academy of Sciences

Kaiming Hu (✉ hkm@mail.iap.ac.cn)

Institute of Atmospheric Physics, Chinese Academy of Sciences <https://orcid.org/0000-0002-9988-5747>

Gang Huang

Institute of Atmospheric Physics Chinese Academy of Sciences

Ya Wang

Institute of Atmospheric Physics Chinese Academy of Sciences

Weichen Tao

Institute of Atmospheric Physics Chinese Academy of Sciences

Research Article

Keywords: El Niño, Anomalous Anticyclone, Intraseasonal variations, Energetics

Posted Date: February 17th, 2021

DOI: <https://doi.org/10.21203/rs.3.rs-195970/v1>

License:  This work is licensed under a Creative Commons Attribution 4.0 International License.

[Read Full License](#)

Version of Record: A version of this preprint was published at Climate Dynamics on August 13th, 2021.

See the published version at <https://doi.org/10.1007/s00382-021-05923-5>.

1 **Intensification and Northward Extension of Northwest Pacific Anomalous**
2 **Anticyclone in El Niño Decaying Mid-Summer: An Energetic Perspective**

3
4
5 Haosu Tang^{1,3}, Kaiming Hu^{1,2}, Gang Huang^{1,2,3}, Ya Wang^{1,3} and Weichen Tao¹

6
7 ¹*State key Laboratory of Numerical Modeling for Atmospheric Sciences and*
8 *Geophysical Fluid Dynamics and Center for Monsoon System Research, Institute of*
9 *Atmospheric Physics, Chinese Academy of Sciences, Beijing, China*

10 ²*Joint Center for Global Change Studies (JCGCS), Beijing 100875, China*

11 ³*University of Chinese Academy of Sciences, Beijing, 100049, China*

12
13 **Submitted to Climate Dynamics**

14 *Corresponding authors: Kaiming Hu and Gang Huang

15 Corresponding author address: Kaiming Hu, IAP/CAS, P.O. Box 9804, Beijing 100029,
16 China; E-mail: hkm@mail.iap.ac.cn and Gang Huang, IAP/CAS, P.O. Box 9804,
17 Beijing 100029, China; E-mail: hg@mail.iap.ac.cn

18

19

Abstract

20 The Northwest Pacific (NWP) anomalous anticyclone (AAC) intensifies and extends
21 northward from El Niño decaying early to mid- summer despite the dissipating sea surface
22 temperature anomalies in the North Indian Ocean, North Atlantic and tropical NWP. The
23 present study investigates these two intraseasonal variations of AAC from the perspective of
24 energetics. The efficiency of dry energy conversion from background mean flow to
25 perturbations in the El Niño decaying mid-summer is high and well explains the intensification
26 of El Niño-induced circulation anomalies over the East Asia (EA)-NWP. The baroclinic energy
27 conversion plays a more dominant role in this process than barotropic energy conversion.
28 Besides, mean state changes over the EA-NWP from early to mid- summer are found in favor
29 of the northward shift of the preferred latitude of the circulation anomalies. Thus, the El Niño-
30 induced circulation anomalies over the EA-NWP are more northward-extended in the later
31 period. Empirical orthogonal function analyses further confirm that the northward extension of
32 El Niño-induced circulation anomalies over the EA-NWP stems from local optimal mode
33 change from early to mid- summer.

34 **Keywords** El Niño; Anomalous Anticyclone; Intraseasonal variations; Energetics

35

Declarations

36
37
38
39
40
41
42
43
44
45
46
47
48
49
50
51
52
53
54
55
56
57
58
59
60
61
62
63

Funding

The work was supported by the National Key R&D Program of China (Fund No: 2019YFA0606703), the Second Tibetan Plateau Scientific Expedition and Research (STEP) program (grant no. 2019QZKK0102), the Strategic Priority Research Program of Chinese Academy of Sciences (XDA20060502), National Natural Science Foundation of China (41775086, 41831175), Key Deployment Project of Centre for Ocean Mega-Research of Science, Chinese Academy of Sciences (COMS2019Q03), and the Youth Innovation Promotion Association of CAS.

Conflicts of interest

The authors declare no competing interests.

Availability of data and material

NCEP-DOE dataset is from <https://psl.noaa.gov/data/gridded/data.ncep.reanalysis2.html>. The CPC Merged Analysis of Precipitation is from <https://psl.noaa.gov/data/gridded/data.cmap.html>. The OLR data is from https://psl.noaa.gov/data/gridded/data.interp_OLR.html. The SST dataset is from <https://www.metoffice.gov.uk/hadobs/hadisst/>.

Code availability

The code associated with this paper is available on request from K. H.

Authors' contributions

H.S., K.H. and G. H. conceived the study, performed the analyses, built the mechanism and wrote the paper.

Ethics approval

Not applicable

Consent to participate

Not applicable

Consent for publication

Not applicable

64 **1. Introduction**

65 Boreal summer is the principal rainy season for East Asia (EA) and Northwest Pacific
66 (NWP). The precipitation here over this period shows immense interannual variability, which
67 is of great socioeconomic importance for the livelihood of over two billion inhabitants (Wang
68 et al. 2001; Huang et al. 2007). El Niño-Southern Oscillation (ENSO) is the leading source for
69 local rainfall variability via giving rise to an anomalous anticyclone (AAC) in the lower
70 troposphere over the Indo-NWP region during El Niño decaying summer (Fu and Ye 1988;
71 Zhang et al. 1996; Wang et al. 2003; Wei et al. 2020). Similar with the Pacific–Japan (PJ)
72 pattern (Nitta 1987) or the East Asia–Pacific (EAP) pattern (Huang and Wu 1989), the El Niño-
73 induced convection anomalies over the NWP could excite a meridional wave train propagating
74 into lower-level extratropical EA during El Niño decaying summer, bringing the influence of
75 El Niño to the extratropics (Kosaka et al. 2013). For instance, the AAC can induce floods at its
76 northern flank via moisture convergence (Huang and Wu 1989; Chang et al. 2000) and
77 droughts in its ridge via subsidence motion (Wang et al. 2000). Besides, the AAC could lead
78 to above-normal surface air temperature (SAT) anomalies in south China through reduced
79 rainfall and downward vertical motion, while the anomalous cyclonic circulation to the north
80 will bring about below-normal SAT anomalies in northeast China through upward vertical
81 motion (Hu et al. 2011). Furthermore, the AAC could decrease tropical cyclones genesis over
82 major parts of the tropical NWP (Du et al. 2011).

83 As for the maintenance mechanisms of the summer NWP AAC, El Niño-induced sea
84 surface temperature (SST) anomalies in the tropical Indian Ocean, tropical Atlantic, and NWP
85 are considered playing an important role. El Niño events generally mature in boreal winter with
86 maximum SST warming in the equatorial eastern Pacific. In the following months, SST
87 anomalies in the equatorial eastern Pacific decay rapidly, but the associated SST anomalies in
88 the tropical Indian Ocean, tropical Atlantic, and NWP can maintain into summer via
89 atmospheric bridge (Klein et al. 1999; Alexander et al. 2002), ocean dynamics (Xie et al. 2002;
90 Huang and Kinter 2002) and air-sea interaction (Wang et al. 2000; Du et al. 2009; Kosaka et
91 al. 2013; Xie et al. 2016). The warming in the tropical Indian Ocean and tropical Atlantic can

92 intensify the summer NWP AAC via the lower-level Ekman divergence invoked by warm
93 equatorial Kelvin wave response (Xie et al. 2009; Rong et al. 2010), while the NWP cooling
94 can intensify the AAC via the atmospheric descending Rossby wave response (Wang et al.
95 2000; Xiang et al. 2013).

96 The fundamental works of the last twenty years successfully explain the formation and
97 maintenance of AAC on the summer seasonal mean timescale, mainly focusing on the role of
98 SST anomalies in three tropical oceans. Nevertheless, the AAC is not only a mode tied to
99 anomalous SST forcing, but also could arise from the atmospheric internal dynamic processes
100 unrelated to SST variability (Kosaka et al. 2013; Zhou et al. 2018; Wang et al. 2018). Recent
101 studies illustrated that the AAC could extract kinetic energy (*KE*) from background mean flow
102 via barotropic energy conversion in the NWP confluence zone (Hu et al. 2019; Wang et al.
103 2020), implying that the impact of SST anomalies on the AAC becomes more efficient under
104 the summer NWP background mean state. However, the EA-NWP mean state changes
105 dramatically throughout the summer. So, how will the AAC change correspondingly?

106 Previous studies reveal an intensification (Xiang et al. 2013) and northward extension (Ye
107 and Lu 2010; Hu et al. 2017; Li and Lu 2018) of the AAC in El Niño decaying summer. As for
108 its mechanism, Ye and Lu (2010) suggested the northward shift of the upper-level westerly jet
109 and NWP subtropical high is responsible for the northward extension of the AAC, which is
110 confirmed by Kosaka and Nakamura (2010) where they conducted two numerical experiments
111 with the westerly jet axis set at 35°N and 50°N, respectively. They found the circulation
112 response is enhanced and displaced poleward in the later experiment. However, this induction
113 confuses people to some extent since the northward shift of the mid-latitude westerly jet is to
114 the disadvantage of Rossby wave propagation from the tropics to extratropics (Tsuyuki and
115 Kurihara 1989). Thus, the concrete process of changes in wave–mean flow interaction over the
116 EA-NWP during El Niño decaying summer entails further comprehension.

117 In this study, we aim to quantify the wave-mean flow interaction processes involved in
118 the intensification and northward extension of AAC during El Niño decaying summer from the
119 view of energetics. The remaining paper is structured as follows. Section 2 describes the data

120 and methods. Section 3 displays the variations of ocean-atmosphere anomalies in each month
121 of El Niño decaying summer. The energy conversion between the AAC and background mean
122 flow is diagnosed in section 4 to illustrate the influence of EA-NWP mean state changes on the
123 AAC. Conclusions and discussion are given in section 5.

124 **2. Data and methods**

125 **a. Datasets**

126 In this study, the monthly and daily mean atmospheric variables are from the National
127 Centers for the Environmental Prediction-Department of Energy (NCEP-DOE) atmospheric
128 reanalysis, which has a horizontal resolution of $2.5^{\circ} \times 2.5^{\circ}$ at 17 height levels (Kanamitsu et al.
129 2002). Pentad-mean precipitation data is from the Climate Prediction Center (CPC) Merged
130 Analysis of Precipitation (Xie and Arkin 1997), given on a $2.5^{\circ} \times 2.5^{\circ}$ horizontal grid. The
131 interpolated daily outgoing longwave radiation (OLR) data is from the National Oceanic and
132 Atmospheric Administration (NOAA) (Liebmann and Smith 1996) and utilized as a proxy for
133 convection, with $2.5^{\circ} \times 2.5^{\circ}$ horizontal resolution. The global gridded monthly SST dataset is
134 from the UK. Met Office Hadley Centre, with $1^{\circ} \times 1^{\circ}$ horizontal resolution (Rayner et al. 2003).
135 The study period is from January 1979 to December 2016.

136 **b. Methods**

137 This study focuses on the interannual variabilities associated with ENSO, so a 9-year
138 running mean has been removed from all monthly and daily datasets to eliminate the decadal
139 variability. The numeral 0 (1) in parentheses denotes the El Niño developing (decaying) years,
140 and the months in this study all refer to those in the Northern Hemisphere. The Niño 3.4 index
141 is defined as the December(0)-February(1) mean SST anomalies averaged over the region $5^{\circ}\text{S}-$
142 5°N and $170^{\circ}\text{W}-120^{\circ}\text{W}$ and D(0)JF(1) is abbreviated as DJF(0). All the statistically significant
143 tests for linear regression are performed using the two-tailed Student's t test.

144 **3. Variations of Ocean-Atmosphere anomalies in El Niño decaying summer**

145 Figures 1 a, d, g show the regression of monthly 850 hPa wind and SAT anomalies in each
146 month of El Niño decaying summer against the standardized DJF(0) Niño3.4 index. The AAC
147 pattern persists throughout the summer, but its spatial structure and amplitude experience

148 pronounced changes in each month. The northern flank of AAC marches northward from 27°N
149 in June(1) to 35°N in July(1) and 38°N in August(1). Besides, the intensity of AAC is observed
150 to increase from June(1) to July(1) and August(1), corresponding with eastward extension of
151 intensified zonally elongated circulation anomalies to the international date line. The AAC
152 intensity is defined as the maximum regressed sea level pressure anomalies around the NWP
153 (10°–20°N, 110°–150°E), and is 19, 123.174 and 94.727 Pa in June(1), July(1) and August(1),
154 respectively.

155 Since the moisture is mainly confined in the lower troposphere, the pattern of regressed
156 vertically integrated moisture fluxes highly resembles the AAC pattern in each month of El
157 Niño decaying summer (Figs. 1b, e, h). Both SAT and rainfall anomalies display a meridional
158 dipole pattern over the EA-NWP, with positive SAT and negative rainfall anomalies in the
159 ridge of the AAC and opposite anomalies at its northern flank. Accompanied with the
160 intensification and northward extension of AAC, the monthly SAT (Figs. 1 a, d, g) and rainfall
161 (Figs. 1 b, e, h) anomalies over EA-NWP also gradually march northward. Specific in China,
162 negative SAT and positive rainfall anomalies are observed around south China in June(1) and
163 move to the mid-latitudes in July(1) and August(1), when the south China is occupied by
164 positive SAT and negative rainfall anomalies. These results indicate that the El Niño-induced
165 circulation and climate anomalies over the EA-NWP have pronounced intraseasonal and
166 month-to-month variations during JJA(1) season.

167 Figures 1 c, f, i show the regression of SST anomalies in each month of El Niño decaying
168 summer against standardized DJF(0) Niño3.4 index. In June(1), there is prominent warming in
169 the tropical North Atlantic, tropical Indian Ocean, South China Sea, and cooling in the
170 subtropical NWP. Such warm-warm-cold SST pattern from west to east is considered
171 responsible for the formation and maintenance of the summer AAC (Xie et al. 2016; Jiang et
172 al. 2017). However, the warming in the tropical North Atlantic, tropical Indian Ocean and
173 cooling in the subtropical NWP are decaying in July(1) and August(1). The SST anomalies
174 averaged over the North Atlantic (NA; 0°–20°N, 60°W–20°W), North Indian Ocean (NIO; 5°–
175 25°N, 40°E–100°E) and NWP (10°–20°N, 150°–170°E) from June(1) to August(1) are

176 calculated. The values are 0.179 (0.216, -0.113), 0.133 (0.197, -0.034), 0.104 (0.171, -
177 0.029) °C for NA (NIO, NWP) in June(1), July(1) and August(1), respectively. Obviously, the
178 weakening warm-warm-cold SST pattern from June(1) to August(1) is not consistent with the
179 intensification of the AAC.

180 To further illustrate the variations of AAC during post-El Niño summer, daily datasets are
181 used to investigate the evolution feature of the AAC. Figure 2 shows the meridional section of
182 pentad-mean precipitation, OLR, and 850 hPa wind anomalies averaged between 110° and
183 150°E regressed against the standardized DJF(0) Niño3.4 index. The northern flank of the AAC
184 leaps from about 30°N in mid-June(1) to 35°N in late July(1), coinciding well with the
185 anomalous rainband. The result indicates that the intraseasonal variations of the AAC does not
186 accurately follow the calendar months, consistent with Hu et al. (2012). Thus, two periods are
187 selected for further analysis. One is early summer(1) that is 15 June(1)-14 July(1), and the other
188 is mid-summer(1) that is 20 July(1)-18 August(1), corresponding to the climatological EA and
189 NWP rainy season, respectively. Since the weakening SST anomalies could not explain the
190 AAC variations, what mechanism involved is responsible for its intensification and northward
191 extension from early to mid- summer(1)?

192 **4. Energetic analyses**

193 To answer the above question, we first examine EA-NWP atmospheric mean state changes
194 from early to mid- summer, then compare the efficiency of energy conversion from background
195 mean flows to the AAC between the two periods.

196 **a. Mean state changes from early to mid- summer**

197 Figures 3a-b present the climatological 850 hPa winds and precipitation. The lower-level
198 winds over the NWP feature a confluence between the westerly monsoon winds from the NIO
199 and easterly trade winds associated with the North Pacific subtropical high. Accompanied with
200 the advancement of the summer westerly monsoon, the confluence zone shifts eastward from
201 early to mid- summer. As for precipitation, the mei-yu/baiu rainband withdraws, and the
202 emergence of the NWP rainband centered approximately at 10°N, 135°E is observed from early
203 to mid- summer. This convective jump (Ueda et al. 1995) is characterized by an abrupt

204 intensification of NWP convective activity in late July (Zhou et al. 2016) and may further exert
205 influence on the change of the Rossby wave source over the NWP. Figures 3c-d show the
206 climatological mean winds at 200 hPa and air temperature at 500 hPa. Accompanied with the
207 northward shift of the solar radiation, high air temperature centers over the EA extend
208 northward from early to mid-summer. The climatological upper-level westerly jet shifts
209 northward from around 40°N in the early summer to around 45°N in the mid-summer according
210 to the thermal wind relation (Lin and Lu 2008). The exit of the westerly jet over Japan weakens
211 in the later period.

212 Previous studies suggest that zonally elongated cyclonic or anticyclonic circulation
213 anomalies over the EA-NWP owe their formation to the configuration of local mean states
214 (Kosaka and Nakamura 2006; 2010; Hirota and Takahashi 2012; Hu et al. 2019). There are
215 five key energy conversion/generation processes at play. First, the lower-level climatological
216 mean winds over the NWP feature a confluence between the westerly monsoon winds and
217 easterly trade winds, which is conducive to zonally-elongated circulation anomalies gaining
218 *KE* from the background mean flow. Second, since the inhomogeneity of the mean flow could
219 energize the perturbations in the midlatitude (Simmons et al. 1983; Branstator 1985), zonally-
220 elongated circulation anomalies tend to gain *KE* from the background mean flow in the exit of
221 the climatological upper-level westerly jet. Third, circulation anomalies tilting westward with
222 height are prone to gain available potential energy (*APE*) from the background mean flow in
223 the upstream of westerly jet exit. Fourth, on the coastal areas of east Asia, the temperature
224 gradient between warm continent and cold ocean is beneficial for circulation anomalies tilting
225 northward with height to gain *APE* from the background mean flow. Fifth, active cumulus
226 convection over the NWP could serve as an important energy source to provide *APE* for the
227 perturbations. The above energy conversion/generation processes are vital to the formation of
228 robust interannual variabilities over the EA-NWP, which are usually characterized by zonally-
229 elongated horizontal pattern and northwestward tilting vertical structure, such as the PJ pattern
230 (Xu et al. 2019; Zhu et al. 2020). As suggested in Figure 3, the NWP background mean states

231 change dramatically from early to mid- summer, then how will these changes lead to variations
 232 in El Niño-induced circulation anomalies over the EA-NWP?

233 **b. Variations in El Niño-induced circulation anomalies from early to mid- summer(1)**

234 Figures 4a-d show the regression of vorticity anomalies at 850 hPa and 200 hPa against
 235 standardized DJF(0) Niño3.4 index and corresponding wave-activity fluxes in the early and
 236 mid- summer. Following Takaya and Nakamura (2001), the wave-activity fluxes are defined
 237 as:

$$238 \quad W = \frac{1}{2|\vec{v}|} \begin{cases} \bar{u}(\psi_x'^2 - \psi' \psi_{xx}') + \bar{v}(\psi_x' \psi_y' - \psi' \psi_{xy}') \\ \bar{u}(\psi_x' \psi_y' - \psi' \psi_{xy}') + \bar{v}(\psi_y'^2 - \psi' \psi_{yy}') \\ f^2/S \{ \bar{u}(\psi_x' \psi_p' - \psi' \psi_{xp}') + \bar{v}(\psi_y' \psi_p' - \psi' \psi_{yp}') \} \end{cases} \quad (1)$$

239 where \vec{V} is the horizontal wind velocity vector, ψ the stream function, f the Coriolis
 240 parameter, $S = (R/p)(R\bar{T}/C_p p - d\bar{T}/dp)$ denotes the static stability, primes and overbars
 241 denote the regressed anomalies against standardized DJF(0) Niño3.4 index and climatological
 242 mean quantities, respectively. The direction of wave-activity fluxes denotes that of local group
 243 velocity of the stationary Rossby wave.

244 In both early and mid- summer(1), the vorticity anomalies mainly feature meridional
 245 wave structure from the NWP to EA, corresponding to lower-tropospheric poleward wave
 246 fluxes. However, the wave fluxes between the two periods exhibit notable differences. The
 247 850hPa wave fluxes in the mid-summer(1) are stronger and extend more northward than those
 248 in the early summer(1) (Figs. 4a-b). Notable upper-level equatorward wave fluxes can be seen
 249 over the subtropical NWP in the mid-summer(1), while they are missing in the early summer(1)
 250 (Figs. 4c-d). The result suggests that the stationary wave activities associated with the AAC
 251 pattern are remarkably different between the two periods. The tropical-extratropical coupling
 252 over the EA-NWP is more robust in the later period, which is attributed to the more prominent
 253 circulation anomalies at high latitudes of EA in the mid-summer(1). Since the AAC is the
 254 tropical lobe of El Niño-induced circulation anomalies over the EA-NWP, hereafter we focus
 255 on the El Niño-induced meridional circulation system rather than the single AAC at low
 256 latitudes.

257 Figures 4e-f show the latitude-height function of 135°E vorticity anomalies in the early
258 and mid- summer regressed onto DJF(0) Nino3.4 index, respectively. In the early summer(1),
259 the vorticity anomalies mainly feature a dipole structure, with phase tilting slight northward
260 with height. The maximum negative and positive anomalies are distributed from 15°-25°N and
261 28°-33°N at lower troposphere, and are 20°-30°N and 30°-45°N at upper troposphere, highly
262 resembling the PJ-related vorticity anomalies (Kosaka and Nakamura 2006). In the mid-
263 summer(1), the vorticity anomalies at 135°E mainly feature a triple structure, with lower-
264 tropospheric negative-positive-negative centers at 20°, 35° and 50°N, respectively, which shift
265 northward by about 5° relative to that in the early summer(1). Apart from the shift of locations,
266 the northward tilting of vorticity anomalies with height in the mid-summer(1) is stronger than
267 those in the early summer(1), suggesting an intensified atmospheric baroclinicity in the later
268 period. Besides, intensified upward wave fluxes appear at high latitudes of EA in the mid-
269 summer(1), implying that the El Niño-induced circulation anomalies tend to extract *APE* from
270 the background mean flow more efficiently in the mid-summer(1) than in the early summer(1).
271 As a result, the three-dimensional meridional circulation system develops stronger and lasts
272 longer in the later period.

273 Figures 4g-h show the longitude-height function of the regressed vorticity anomalies at 40°
274 and 45°N where the westerly jet cores in the early and mid- summer(1) are located, respectively.
275 Significant positive vorticity anomalies tilt slightly westward with height in the upstream of
276 westerly jet exit while eastward in the downstream in both early and mid- summer(1). Besides,
277 there are pronounced upward (downward) wave fluxes associated with the westward (eastward)
278 inclination in the mid-summer(1), suggesting an intensified upward propagation of wave
279 energy in this period. Since the energy conversion efficiency depends on the relative position
280 between background mean flow and the El Niño-induced circulation anomalies, we further
281 investigate the concrete energy conversion processes in the next part.

282 **c. Mechanisms for the intensification of El Niño-induced circulation anomalies**

283 Following Kosaka and Nakamura (2006), the barotropic energy conversion (*CK*) from the
284 background mean flow to perturbations can be given by

285
$$CK = \underbrace{\frac{(v'^2 - u'^2)}{2} \left(\frac{\partial \bar{u}}{\partial x} - \frac{\partial \bar{v}}{\partial y} \right)}_{CK_x} - \underbrace{u'v' \left(\frac{\partial \bar{u}}{\partial y} + \frac{\partial \bar{v}}{\partial x} \right)}_{CK_y} \quad (2)$$

286 where u and v denote the zonal and meridional winds, respectively. The baroclinic energy
 287 conversion (CP) from the background mean flow to perturbations is defined as

288
$$CP = \underbrace{\frac{Rf}{sp} u' t' \frac{\partial \bar{v}}{\partial p}}_{CP_x} - \underbrace{\frac{Rf}{sp} v' t' \frac{\partial \bar{u}}{\partial p}}_{CP_y} \quad (3)$$

289 where R denotes the gas constant, t the temperature, C_p the specific heat at constant
 290 pressure, and P the pressure. To objectively measure the efficiency of CK and CP in
 291 replenishing the El Niño-induced circulation anomalies over the EA-NWP, we calculate dry
 292 energy conversion time scale: $\tau_{dry} = [KE + APE]/[CK + CP]$, where the bracket represents
 293 the area mean of 0–60°N, 110°–150°E. The qualitative result does not change too much even
 294 if the chosen area is slightly enlarged or shrank. Positive value less than 30 days indicates the
 295 corresponding process is efficient enough to maintain the El Niño-induced circulation
 296 anomalies over the EA-NWP, while value more than 30 days indicates the process is beneficial
 297 but not efficient. Negative value suggests that the process is detrimental to the maintenance of
 298 the El Niño-induced circulation anomalies. The τ_{dry} is 7.241 and 3.804 days in early and
 299 mid- summer(1), respectively (Table 1), suggesting the El Niño-induced circulation anomalies
 300 over the EA-NWP can extract dry energy from the background mean flow more efficiently in
 301 the later period. As a result, the NWP AAC intensifies in this period. We further investigate
 302 the relative role played by CK and CP in the following paragraphs.

303 Figure 5 shows the CK at 850 hPa and 200 hPa during early and mid- summer(1). At 850
 304 hPa, pronounced positive CK lies on the climatological zonal winds' confluence zone
 305 ($\partial \bar{u}/\partial x < 0$) from the South China Sea to the east of the Philippine in both periods (Figs. 5a-
 306 b). The fixed position of positive CK by the NWP convergent background mean flow could
 307 explain, at least in part, why the southern flank of AAC is anchored around 10°N in both early
 308 and mid- summer(1) (Fig. 2). Further analysis suggests that CK_x [especially $-(u'^2/2)(\partial \bar{u}/\partial x)$]
 309 plays a dominant role in inducing lower-level CK due to the zonally elongated shape of AAC

310 ($u'^2 > v'^2$), emphasizing the importance of interaction between background zonal mean flow
311 and circulation anomalies in triggering the AAC (figure not shown).

312 At 200 hPa, the positive and negative CK adjoin one another around the exit of the upper-
313 level westerly jet ($\partial\bar{u}/\partial x < 0$). The westerly jet advances northward and weakens from early
314 to mid- summer(1) and so does the CK along the westerly jet (Figs. 5c-d). Another conspicuous
315 positive CK center is found in the Okhotsk sea in the mid-summer(1) (Fig. 5d). Since the
316 direction of the wave fluxes and momentum fluxes is opposite with each other, the salient
317 equatorward wave fluxes over the Okhotsk sea (Fig. 4d) denote strong poleward momentum
318 fluxes ($u'v' > 0$). Thus, these poleward momentum fluxes to the north of the westerly jet core
319 ($\partial\bar{u}/\partial y < 0$) favor the formation of positive CK [$-u'v'(\partial\bar{u}/\partial y) > 0$].

320 The barotropic energy conversion time scale is defined as $\tau_{CK} = [KE]/[CK]$. The τ_{CK} is
321 9.538 and 15.574 days at 850 hPa, 2.756 and 7.729 days at 200 hPa, and 5.563 and 7.58 days
322 when integrated vertically in the early and mid- summer(1), respectively (Table 1). The result
323 indicates that CK is efficient in both early and mid- summer(1), but more efficient in the former
324 period. That is to say, the El Niño-induced circulation anomalies over the EA-NWP can more
325 efficiently gain barotropic energy from the background mean flow in the early summer(1) than
326 in the mid-summer(1). Thus, CK plays a negative role in the intensification of El Niño-induced
327 circulation anomalies over the EA-NWP. On the other hand, it should be noted that Eq. (1)
328 dismisses the redistribution of KE from one area to the other, so the simple area average may
329 import errors. However, this method is still a good way to preliminarily quantify the wave-
330 mean flow interaction.

331 Figure 6 shows the vertically integrated CP and climatological mean temperature at 500
332 hPa during early and mid- summer(1). The most pronounced positive CP over the EA in the
333 early summer(1) is situated from Korean Peninsula to the Japan Sea. The positive CP
334 remarkably intensifies and advances northward to the Far East in the mid-summer(1), with its
335 shape changing from the zonally-elongated to northeastward-slanted. We further decompose
336 CP into CP_x and CP_y (Figs. 6c-f). CP_x makes marginal contributions in the early summer(1)
337 but comes into play in the mid-summer(1). The positive CP_x over the Okhotsk sea in the later

338 period facilitates the positive CP , resulting from an intensified interaction between eastward
 339 heat transport ($u't' > 0$) and thermal contrast between the warm continent and cold ocean
 340 ($\partial\bar{v}/\partial p > 0$). Positive CP_y is of paramount importance in positive CP . Since the direction of
 341 the vertical wave fluxes and heat fluxes is the same, the salient upward wave fluxes denote
 342 strong poleward heat fluxes ($v't' > 0$). Due to the existence of meridional temperature
 343 gradient, $\partial\bar{u}/\partial p < 0$ exists in mid-latitudes of EA. Thus, the structure of westward tilt with
 344 height ($-v't' < 0$) is to the benefit of positive CP_y ($-v't'(\partial\bar{u}/\partial p) > 0$). The baroclinicity
 345 of the atmosphere is pronounced at mid-high latitudes of EA, leading to stronger CP_y in the
 346 mid-summer(1). As a result, the El Niño-induced circulation anomalies over the EA-NWP in
 347 the later period are robust.

348 The efficiency of CP in replenishing the local APE of perturbations is measured by $\tau_{CP} =$
 349 $[APE]/[CP]$. The τ_{CP} is 11.689 and 1.618 days in early and mid- summer(1), respectively
 350 (Table 1), indicating that CP can energize the El Niño-induced circulation anomalies much
 351 more effectively in the later period. Thus, CP may account for why the El Niño-induced
 352 circulation anomalies intensify when the anomalous SST forcing weakens in the mid-
 353 summer(1).

354 **d. Mechanisms for the northward extension of El Niño-induced circulation anomalies**

355 In the last section, we investigate the mechanisms for intensification of El Niño-induced
 356 circulation anomalies over the EA-NWP in mid-summer(1) via comparison of energy
 357 conversion efficiency in two periods. In this part, we further discuss the mechanisms for the
 358 northward extension of El Niño-induced circulation anomalies over the EA-NWP. Kosaka and
 359 Nakamura (2010) demonstrated that the mode which can extract energy from background mean
 360 states most efficiently is the one most sustainable. Thus, every mode has a preferred latitude or
 361 longitude phase. Here, we analyze whether the El Niño-induced circulation anomalies over the
 362 EA-NWP during the early and mid- summer(1) are the modes which can maximize the
 363 efficiency of energy conversion.

364 Following Kosaka and Nakamura (2010), we artificially displace the El Niño-induced
 365 circulation anomalies over the EA-NWP by every 5° in latitude, while the climatological

366 background mean states are fixed. Through moving the modes meridionally, we aim to
367 examine whether these modes are the dynamic modes inherent in the background mean states.
368 Table 2 gives the time scales with which the El Niño-induced circulation anomalies could gain
369 energy after the anomalous circulation pattern is shifted meridionally relative to its original
370 location. The result shows that the El Niño-induced circulation anomalies over the EA-NWP
371 gain dry energy from background mean flow most efficiently at the original latitude in both
372 two periods. The El Niño-induced circulation anomalies in the early and mid- summer(1) both
373 are the optimal modes, and their locations are fixed meridionally according to the background
374 mean flow. Background mean flow shifts northward from the early to mid- summer(1) and
375 leads to resultant northward extension of anomalous meridional circulation system.

376 On the other hand, it should be noted that the artificially displaced circulation anomalies
377 no longer meet the thermal or vorticity balance, so we verify the results by additional empirical
378 orthogonal function (EOF) analyses. We perform EOF analyses on the 850 hPa vorticity
379 anomalies over the EA-NWP (10° - 60° N, 100° - 160° E) from 1979 to 2016 in the early and mid-
380 summer, respectively (Figs. 7a, b). The domain of EOF analysis is same as that in Kubota et
381 al. (2016). The leading EOF modes in the early and mid- summer explain 18.094% and 20.21%,
382 respectively, both are well separated with other modes by the criterion of North et al. (1982).
383 The EOF1 modes feature an AAC pattern over the NWP in early and mid- summer, while
384 extending more northward in the later period. Since the EOF1 normally captures the dominant
385 mode of the interannual variability, the result suggests that the circulation anomalies over the
386 EA-NWP tend to occur in a more northward position in the mid-summer. PC1s in the early and
387 mid- summer are highly correlated with DJF(0) Niño3.4 index ($r = 0.46$ and 0.466 , respectively,
388 both $p < 0.01$, $n = 38$).

389 We further use partial correlation method to remove the influence of ENSO, and perform
390 EOF analyses again on the residues in the early and mid- summer(1), respectively (Figs. 7c, d).
391 Thus, we get the dominant mode of atmospheric interannual variability over the EA-NWP
392 independent of ENSO. The patterns are almost the same as those presented in Figs. 7a, b, and
393 the correlations between PC1s in the early and mid- summer and DJF(0) Niño3.4 index are

394 both nearly zero this time. The result further confirms that the northward extension of El Niño-
395 induced circulation anomalies over the EA-NWP stems from local optimal internal mode
396 change from early to mid- summer, which is independent of ENSO.

397 **5. Conclusions and discussion**

398 **a. Conclusions**

399 We have investigated the intraseasonal variations of the AAC during El Niño decaying
400 summer and explained these phenomena from the perspective of energetics. It is noted that the
401 El Niño-induced circulation anomalies over the EA-NWP are stronger and more northward-
402 extended in in July(1) and August(1) than in June(1), while the decaying SST anomalies over
403 the NIO, NA and NWP could not account for this shift (Fig. 1). Based on daily datasets, we
404 further divide the study period into early summer(1) [15 June(1)-14 July(1)] and mid-summer(1)
405 [20 July(1)-18 August(1)], which is more accurate than month division since the most
406 pronounced AAC transition occurs in late July(1) (Fig. 2).

407 Then we diagnose the El Niño-induced circulation anomalies over the EA-NWP from the
408 perspective of energetics and draw the following three conclusions. First, El Niño will induce
409 more prominent circulation anomalies at high latitudes of EA in the mid-summer(1) than in the
410 early summer(1), associated with more salient lower-level poleward wave fluxes originating
411 from the NWP and injecting upward in the upstream of westerly jet exit in the later period (Fig.
412 4). It suggests the tropical-extratropical coupling over the EA-NWP is more robust in the mid-
413 summer(1) from the view of atmospheric wave. Second, dry energy conversion from the
414 background mean flow to perturbations over the NWP-EA is more efficient in the El Niño
415 decaying mid-summer than in the early summer, well explaining the intensification of El Niño-
416 induced circulation anomalies (Table 1). CP (especially CP_y) plays a more dominant role in
417 this process than CK (Figs. 5,6). Third, through artificially displacing the El Niño-induced
418 circulation anomalies over the EA-NWP in the meridional direction, it is found that only at the
419 original latitude can the El Niño-induced circulation anomalies gain dry energy from the
420 background mean flow most efficiently (Table 2), suggesting the original latitude is the
421 preferred latitude of the El Niño-induced circulation anomalies. Mean state changes over the

422 EA-NWP from early to mid- summer favor the northward shift of the preferred latitude of the
423 circulation anomalies. Thus, the El Niño-induced circulation anomalies over the EA-NWP are
424 more northward-extended in the later period. Additional EOF analyses further confirm that the
425 northward extension of El Niño-induced circulation anomalies over the EA-NWP stems from
426 local optimal internal mode change from early to mid- summer, which is independent of ENSO
427 (Fig. 7).

428 **b. Discussion**

429 In this study, we calculate CK and CP to explain the intensification of the AAC. On the
430 other hand, we use perturbation displacement method and EOF to discover the optimal internal
431 mode over the EA-NWP and further explain the northward extension of the AAC. In fact, the
432 above two points of view are not independent but complementary to each other. The northward
433 shift of CK and CP in the mid-summer(1) (Figs. 5,6) can also explain the northward extension
434 of the AAC while the enhanced optimal internal mode in the mid-summer (Figs. 7a,b) can also
435 elucidate the intensification of the AAC. Since every method has its limitation, this cross-
436 validation thought is frequently used in the energetics to increase the reliability of the
437 conclusion (Kosaka and Nakamura 2010).

438 Besides, although the results shown in this study are confined to NWP AAC during El
439 Niño decaying summer, local optimal mode change due to mean state changes in the mid-
440 summer may render all intraseasonal to monthly perturbations over the EA-NWP stronger and
441 more northward-extended, expanding the implications of this study. It can also be inferred that
442 the extratropical circulation of EA is of a higher predictability in the mid-summer since the
443 tropical-extratropical coupling is stronger in this period. The pioneering work of Tsuyuki and
444 Kurihara (1989) suggested that the intraseasonal PJ pattern is inclined to be more energetic in
445 the mid-summer than in the early summer, which also supports the conjecture.

446 Furthermore, it should be noted that the vertical shear of background zonal mean flow is
447 important for the transformation from the baroclinic structure into a barotropic structure to
448 convey the thermally induced baroclinic disturbances to the extratropics (e.g., Wang and Xie
449 1996). As suggested by Lu (2004), the easterly shear of background zonal mean flow over the

450 NWP is robust in August while nearly neutral in June, thus the El Niño-induced local
451 convection anomalies could induce stronger circulation anomalies in mid-high latitudes of EA
452 in the mid-summer(1) (Figs. 4a-d).

453 Last but not the least, it's worth noting that the moist process is also of great significance
454 to amplify the AAC (Kosaka and Nakamura 2006; Hu et al. 2019), while the present study
455 dismisses detailed analysis of this process. Since the climatological mean precipitation over
456 the NWP enhances from early to mid- summer (Figs. 3a-b; Xiang et al. 2013), the local
457 atmospheric response becomes more sensitive to external forcing (Wu et al. 2010), thus an
458 intensified AAC will ensue. Since the AAC is interactively correlated with the anomalous
459 negative precipitation in its ridge (Xie et al. 2009) and anomalous rainband at its northern flank
460 (Lu and Lin 2009; Matsumura et al. 2015), it is difficult to truly separate circulation from
461 convection and investigate the causality between each other, which deserves future studies.

462

463 **Acknowledgements:** The work was supported by the National Key R&D Program of
464 China (Fund No: 2019YFA0606703), the Second Tibetan Plateau Scientific Expedition
465 and Research (STEP) program (grant no. 2019QZKK0102), the Strategic Priority
466 Research Program of Chinese Academy of Sciences (XDA20060502), National Natural
467 Science Foundation of China (41775086, 41831175), Key Deployment Project of
468 Centre for Ocean Mega-Research of Science, Chinese Academy of Sciences
469 (COMS2019Q03), and the Youth Innovation Promotion Association of CAS.
470

471 **References**

- 472 Alexander MA, Bladé I, Newman M, Lanzante JR, Lau NC, Scott JD (2002) 2002: The
473 atmospheric bridge: The influence of ENSO teleconnections on air–sea interaction over
474 the global oceans. *J Climate* 15 (16):2205-2231
- 475 Branstator G (1985) Analysis of General Circulation Model Sea-Surface Temperature
476 Anomaly Simulations Using a Linear Model. Part I: Forced Solutions. *J Atmos Sci* 42
477 (21):2225–2241
- 478 Chang CP, Zhang Y, Li T (2000) Interannual and Interdecadal Variations of the East Asian
479 Summer Monsoon and Tropical Pacific SSTs. Part I: Roles of the Subtropical Ridge. *J*
480 *Clim* 13 (24):4310-4325
- 481 Du Y, Xie S-P, Huang G, Hu K (2009) Role of Air–Sea Interaction in the Long Persistence of
482 El Niño–Induced North Indian Ocean Warming. *J Clim* 22 (8):2023-2038
- 483 Du Y, Yang L, Xie SP (2011) Tropical Indian Ocean Influence on Northwest Pacific Tropical
484 Cyclones in Summer Following Strong El NiñoEl Niño. *J Clim* 24 (1):315-322
- 485 Fu C, Ye D (1988) The Tropical Very Low-Frequency Oscillation on Interannual Scale. *Adv*
486 *Atmos Sci* 5 (3):369–388
- 487 Hirota N, Takahashi M (2012) A tripolar pattern as an internal mode of the East Asian summer
488 monsoon. *Clim Dyn* 39:2219–2238
- 489 Hu K, Huang G, Huang R (2011) The Impact of Tropical Indian Ocean Variability on Summer
490 Surface Air Temperature in China. *J Clim* 24 (20):5365-5377
- 491 Hu K, Huang G, Qu X, Huang R (2012) The impact of Indian Ocean variability on high
492 temperature extremes across the southern Yangtze River valley in late summer. *Adv*
493 *Atmos Sci* 29 (1):91-100
- 494 Hu K, Huang G, Xie S-P, Long S-M (2019) Effect of the mean flow on the anomalous
495 anticyclone over the Indo-Northwest Pacific in post-El Niño summers. *Clim Dyn* 53
496 (9-10):5725-5741
- 497 Hu K, Xie S-P, Huang G (2017) Orographically Anchored El Niño Effect on Summer Rainfall
498 in Central China. *J Clim* 30 (24):10037-10045

- 499 Huang B, Kinter JL III (2002) Interannual variability in the tropical Indian Ocean. *J Geophys*
500 *Res* 107(C11):3199
- 501 Huang R, Chen J, Huang G (2007) Characteristics and Variations of the East Asian Monsoon
502 System and Its Impacts on Climate Disasters in China. *Adv Atmos Sci* 24:993–1023
- 503 Huang R, Wu Y (1989) The Influence of ENSO on the Summer Climate Change in China and
504 Its Mechanism. *Adv Atmos Sci* 6 (1):21-32
- 505 Jiang W, Huang G, Hu K, Wu R, Gong H, Chen X, Tao W (2017) Diverse Relationship
506 between ENSO and the Northwest Pacific Summer Climate among CMIP5 Models:
507 Dependence on the ENSO Decay Pace. *J Clim* 30 (1):109-127
- 508 Kanamitsu M, Ebisuzaki W, Woollen J, Yang SK, Hnilo JJ, Fiorino M, Potter GL (2002)
509 NCEP–DOE AMIP-II Reanalysis (R-2). *Bull Am Meteorol Soc* 83 (11):1631-1643
- 510 Klein SA, Soden BJ, Lau NC (1999) Remote Sea Surface Temperature Variations during
511 ENSO: Evidence for a Tropical Atmospheric Bridge. *J Clim* 12 (4):917-932
- 512 Kosaka Y, Nakamura H (2006) Structure and dynamics of the summertime Pacific–Japan
513 teleconnection pattern. *Q J R Meteorol Soc* 132 (619):2009-2030
- 514 Kosaka Y, Nakamura H (2010) Mechanisms of Meridional Teleconnection Observed between
515 a Summer Monsoon System and a Subtropical Anticyclone. Part I: The Pacific–Japan
516 Pattern. *J Clim* 23 (19):5085-5108
- 517 Kosaka Y, Xie SP, Lau NC, Vecchi GA (2013) Origin of seasonal predictability for summer
518 climate over the Northwestern Pacific. *Proc Natl Acad Sci* 110 (19):7574-7579
- 519 Kubota H, Kosaka Y, Xie S-P (2016) A 117-year long index of the Pacific-Japan pattern with
520 application to interdecadal variability. *Int J Climatol* 36 (4):1575–1589
- 521 Li X, Lu R (2018) Subseasonal Change in the Seesaw Pattern of Precipitation between the
522 Yangtze River Basin and the Tropical Western North Pacific during Summer. *Adv*
523 *Atmos Sci* 35 (10):1231–1242
- 524 Liebmann B, Smith CA (1996) Description of a Complete (Interpolated) Outgoing Longwave
525 Radiation Dataset. *Bull Am Meteorol Soc* 77:1275-1277

526 Lin Z, Lu R (2008) Abrupt Northward Jump of the East Asian Upper-Tropospheric Jet Stream
527 in Mid-Summer. *J Meteorol Soci Jpn* 86 (6):857-866

528 Lu R (2004) Associations among the Components of the East Asian Summer Monsoon System
529 in the Meridional Direction. *J Meteorol Soci Jpn* 82 (1):155-165

530 Lu R, Lin Z (2009) Role of Subtropical Precipitation Anomalies in Maintaining the
531 Summertime Meridional Teleconnection over the Western North Pacific and East Asia.
532 *J Clim* 22 (8):2058-2072

533 Matsumura S, Sugimoto S, Sato T (2015) Recent Intensification of the Western Pacific
534 Subtropical High Associated with the East Asian Summer Monsoon. *J Clim* 28
535 (7):2873-2883

536 Nitta T (1987) Convective activities in the tropical western Pacific and their impact on the
537 northern hemisphere summer circulation. *J Meteorol Soci Jpn* 65:165–171

538 North GR, Bell TL, Cahalan RF, Moeng FJ (1982) Sampling errors in the estimation of
539 empirical orthogonal functions. *Mon Weather Rev* 110 (7):699–706

540 Rayner N, Parker D, Horton E, Folland C, Alexander L, Rowell D, Kent E, Kaplan A (2003)
541 Global analyses of sea surface temperature, sea ice, and night marine air temperature
542 since the late nineteenth century. *J Geophys Res Atmos* 108 (D14):4407

543 Rong X, Zhang R, Li T (2010) Impacts of Atlantic sea surface temperature anomalies on Indo-
544 East Asian summer monsoon-ENSO relationship. *Chin Sci Bull* 55 (22):2458–2468

545 Simmons A, Wallace J, Branstator G (1983) Barotropic wave propagation and instability, and
546 atmospheric teleconnection patterns. *J Atmos Sci* 40:1363–1392

547 Takaya K, Nakamura H (2001) A Formulation of a Phase-Independent Wave-Activity Flux for
548 Stationary and Migratory Quasigeostrophic Eddies on a Zonally Varying Basic Flow.
549 *J Atmos Sci* 58 (6):608-627

550 Tsuyuki T, Kurihara K (1989) Impact of Convective Activity in the Western Tropical Pacific
551 on the East Asian Summer Circulation. *J Meteorol Soci Jpn* 67 (2):231-247

- 552 Ueda H, Yasunari T, Kawamura R (1995) Abrupt Seasonal Change of Large-Scale Convective
553 Activity over the Western Pacific in the Northern Summer. *J Meteorol Soci Jpn* 73
554 (4):795-809
- 555 Wang B, Xie X (1996) Low-Frequency Equatorial Waves in Vertically Sheared Zonal Flow.
556 Part I: Stable Waves. *J Atmos Sci* 53 (23):449-467
- 557 Wang B, Wu R, Fu X (2000) Pacific-East Asian Teleconnection: How Does ENSO Affect East
558 Asian Climate? *J Clim* 13 (9):1517-1536
- 559 Wang B, Wu R, Lau KM (2001) Interannual Variability of the Asian Summer Monsoon:
560 Contrasts between the Indian and the Western North Pacific–East Asian Monsoons. *J*
561 *Clim* 14 (20):4073-4090
- 562 Wang B, Wu R, Li T (2003) Atmosphere–Warm Ocean Interaction and Its Impacts on Asian–
563 Australian Monsoon Variation. *J Clim* 16 (8):1195-1211
- 564 Wang C-Y, Xie S-P, Kosaka Y (2018) Indo-Western Pacific Climate Variability: ENSO
565 Forcing and Internal Dynamics in a Tropical Pacific Pacemaker Simulation. *J Clim* 31
566 (24):10123–10139
- 567 Wang X, Xie SP, Guan Z (2020) Atmospheric Internal Variability in the Summer Indo–
568 Northwestern Pacific: Role of the Intraseasonal Oscillation. *J Clim* 33 (8):3395–3410
- 569 Wei, K., C. Ouyang, H. Duan, Y. Li, M. Chen, J. Ma, H. An and S. Zhou (2020) Reflections
570 on the catastrophic 2020 yangtze river basin flooding in southern china. *The Innovation*
571 2(1):100038
- 572 Wu B, Li T, Zhou T (2010) Relative Contributions of the Indian Ocean and Local SST
573 Anomalies to the Maintenance of the Western North Pacific Anomalous Anticyclone
574 during the El Niño Decaying Summer. *J Clim* 23 (11):2974-2986
- 575 Xiang B, Wang B, Yu W, Xu S (2013) How can anomalous western North Pacific Subtropical
576 High intensify in late summer? *Geophys Res Lett* 40 (10):2349-2354
- 577 Xie P, Arkin PA (1997) Global precipitaion: A 17-year monthly analysis based on gauge
578 observations, satellite estimates. *Bull Am Meteorol Soc* 78 (11):2539-2558

579 Xie S-P, Hu K, Hafner J, Tokinaga H, Du Y, Huang G, Sampe T (2009) Indian Ocean Capacitor
580 Effect on Indo–Western Pacific Climate during the Summer following El Niño. *J Clim*
581 22 (3):730-747

582 Xie S-P, Kosaka Y, Du Y, Hu K, Chowdary JS, Huang G (2016) Indo-western Pacific ocean
583 capacitor and coherent climate anomalies in post-ENSO summer: A review. *Adv Atmos*
584 *Sci* 33 (4):411-432

585 Xie SP, Annamalai H, Schott FA, McCreary JP (2002) Structure and Mechanisms of South
586 Indian Ocean Climate Variability. *J Clim* 15 (8):864–878

587 Xu P, Wang L, Chen W, Feng J, Liu Y (2019) Structural Changes in the Pacific–Japan Pattern
588 in the Late 1990s. *J Clim* 32 (2):607-621

589 Ye H, Lu R (2010) Subseasonal Variation in ENSO-Related East Asian Rainfall Anomalies
590 during Summer and Its Role in Weakening the Relationship between the ENSO and
591 Summer Rainfall in Eastern China since the Late 1970s. *J Clim* 24 (9):2271-2284

592 Zhang R, Sumi A, Kimoto M (1996) Impact of El NinoEl Niño on the East Asian monsoon :
593 A diagnostic study of the '86/87 and '91/92 events. *J Meteorol Soci Jpn* 74 (1):49-62

594 Zhou W, Xie S-P, Zhou Z-Q (2016) Slow Preconditioning for the Abrupt Convective Jump
595 over the Northwest Pacific during Summer. *J Clim* 29 (22):8103-8113

596 Zhou Z-Q, Xie S-P, Zhang G, Zhou W (2018) Evaluating AMIP Skill in Simulating Interannual
597 Variability over the Indo-Western Pacific. *J Clim* 31 (6):2253–2265

598 Zhu Y, Wen Z, Guo Y, Chen R, Li X, Qiao Y (2020) The characteristics and possible growth
599 mechanisms of the quasi-biweekly Pacific–Japan teleconnection in Boreal Summer.
600 *Clim Dyn* 55:3363–3380
601

602 **Figure Captions:**

603 **Figure 1.** (Left) 850 hPa wind (vectors) and SAT (colors) anomalies, (middle) vertically
604 integrated (from the surface to 200 hPa) moisture fluxes (vectors) and their divergence (colors),
605 (right) SST anomalies (colors) in (a, b, c) June, (d, e, f) July, (g, h, i) August regressed against
606 standardized DJF(0) Niño3.4 index for 1978/79–2015/16. Vectors only exceeding the 90%
607 confidence level are shown and dots indicate that the anomalies are significant at the 90%
608 confidence level. The hatched areas from west to east (c) indicate NA, NIO and NWP,
609 respectively.

610 **Figure 2.** 850 hPa wind (vectors, shown only exceeding the 90% confidence level),
611 precipitation (colors, dots indicate that the anomalies are significant at the 90% confidence
612 level) and OLR (contours for ± 2 , ± 4 , ± 6 , ± 8) anomalies averaged between 110° – 150° E
613 regressed against standardized DJF(0) Niño3.4 index for 1978/79–2015/16. Solid and dashed
614 contours represent negative and positive convection anomalies, respectively. Early summer(1)
615 is defined as 15 June(1)–14 July(1) and mid-summer(1) 20 July(1)–18 August(1).

616 **Figure 3.** Climatological mean horizontal winds (vectors) at 850 hPa (a, b) and 200 hPa (c, d),
617 superimposed on the climatological mean precipitation (colors; a, b) and air temperature at 500
618 hPa (colors; c, d) in the early and mid- summer. Climatological mean zonal winds are also
619 overlaid (contours for 15, 20, 25, 30 m/s; c, d).

620 **Figure 4.** Relative vorticity anomalies (colors, dots indicate that the anomalies are significant
621 at the 90% confidence level) at (a, b) 850 hPa and (c, d) 200 hPa in (a, c) early summer, (b, d)
622 mid-summer regressed against standardized DJF(0) Niño3.4 index for 1978/79–2015/16.
623 Meridional section of regressed vorticity anomalies (colors) at (e, f) 135° E in the early and
624 mid-summer(1), respectively. Zonal section of regressed vorticity anomalies (colors) at (g) 40°
625 and (h) 45° N in the early and mid-summer(1), respectively. Vectors denote the corresponding
626 wave fluxes.

627 **Figure 5.** Barotropic energy conversion CK at 850 hPa and 200 hPa during El Niño decaying
628 early summer (a, c) and mid-summer (b, d).

629 **Figure 6.** Vertically integrated (1000-200 hPa) baroclinic energy conversion CP (colors) and
630 climatological mean temperature at 500 hPa (contours, °C) during El Niño decaying early
631 summer (a) and mid-summer (b). Also shown are CP_x and CP_y in the Eq. (2) during El Niño
632 decaying early summer (c, e) and mid-summer (d, f).

633 **Figure 7.** 850 hPa wind anomalies (vectors) regressed against standardized PC1 of the EOF
634 analyses performed on standardized 850 hPa vorticity anomalies over the EA-NWP (10°-60°N,
635 100°–160°E) during El Niño decaying early summer (a) and mid-summer (b). c (d) is the same
636 as a (b) but on the 850 hPa vorticity anomalies independent of ENSO. Vectors only exceeding
637 the 90% confidence level are shown.

638

639 **Table 1.** Time scales (days) with which the El Niño-induced circulation anomalies could gain
640 energy from barotropic energy conversion (*CK*), baroclinic energy conversion (*CP*) and dry
641 energy conversion (*CK + CP*) during El Niño decaying early summer and mid-summer. The
642 eddy energy and energy conversions are integrated vertically from 1000 to 200 hPa and then
643 horizontally over 0-60°N, 110°-150°E.

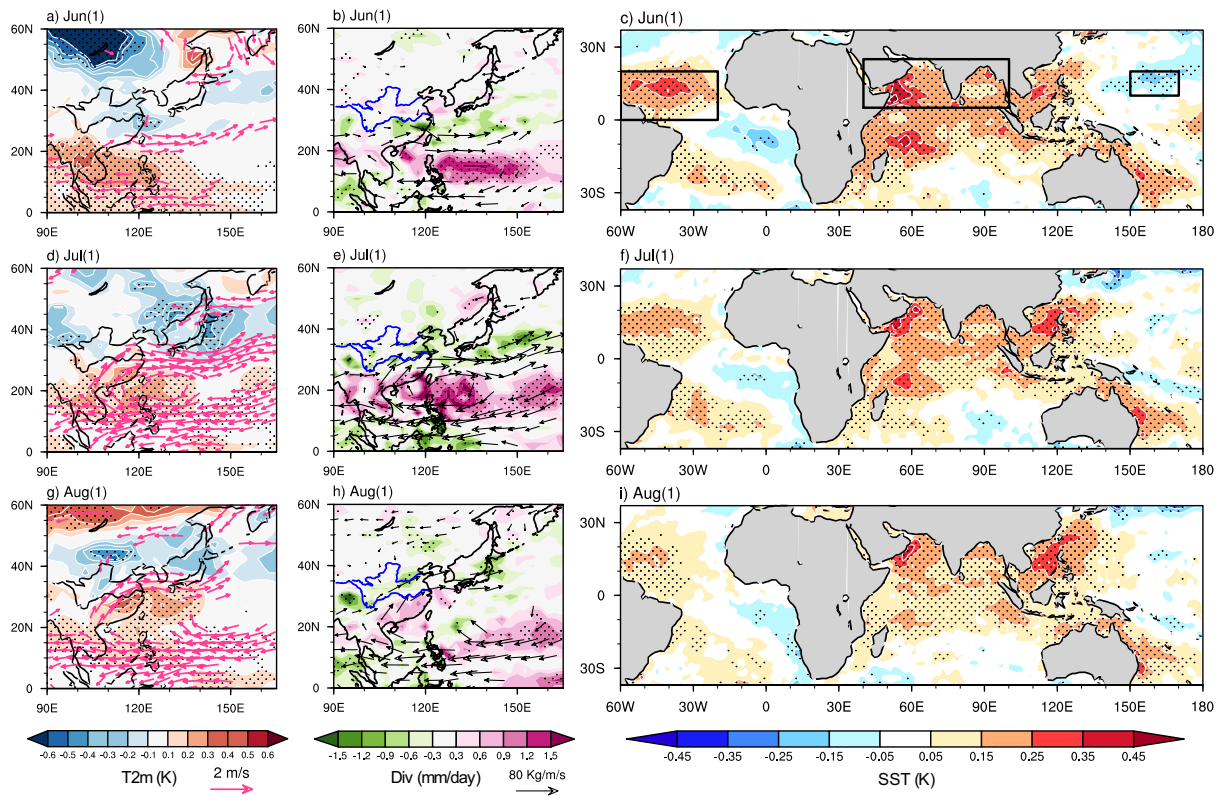
0-60°N, 110°-150°E		Early summer(1)	Mid-summer(1)
τ_{CK}	850 hPa	9.538	15.574
	200 hPa	2.756	7.729
	Vertical integral	5.659	7.636
τ_{CP}	Vertical integral	11.253	1.597
τ_{dry}	Vertical integral	7.15	3.797

644

645 **Table 2.** Time scales (days) with which the El Niño-induced circulation anomalies could gain
646 energy after the circulation pattern is shifted meridionally relative to its original location. The
647 eddy energy is calculated from the original circulation pattern and integrated over 0-60°N,
648 100°-160°E, whereas the energy conversions are integrated over the new domain shifted with
649 the circulation pattern. Both the eddy energy and energy conversions are integrated vertically
650 from 1000 to 200 hPa before integrated horizontally. The efficiencies in the original latitude
651 are highlighted in shadow.

	τ_{CK}		τ_{CP}		τ_{dry}	
	Early summer(1)	Mid-summer(1)	Early summer(1)	Mid-summer(1)	Early summer(1)	Mid-summer(1)
15° northward	-7.976	-45.036	-10.07	2.068	-8.738	8.851
10° northward	-9.898	217.056	-11.12	1.908	-10.376	6.969
5° northward	29.903	12.993	36.744	1.766	32.436	4.814
Original	5.659	7.636	11.253	1.597	7.15	3.797
5° southward	6.24	9.331	-43.246	1.595	11.996	4.063
10° southward	19.872	141.978	-3.995	1.826	-13.203	6.597
15° southward	-5352.58	-10.994	-2.322	2.506	-5.533	24.979

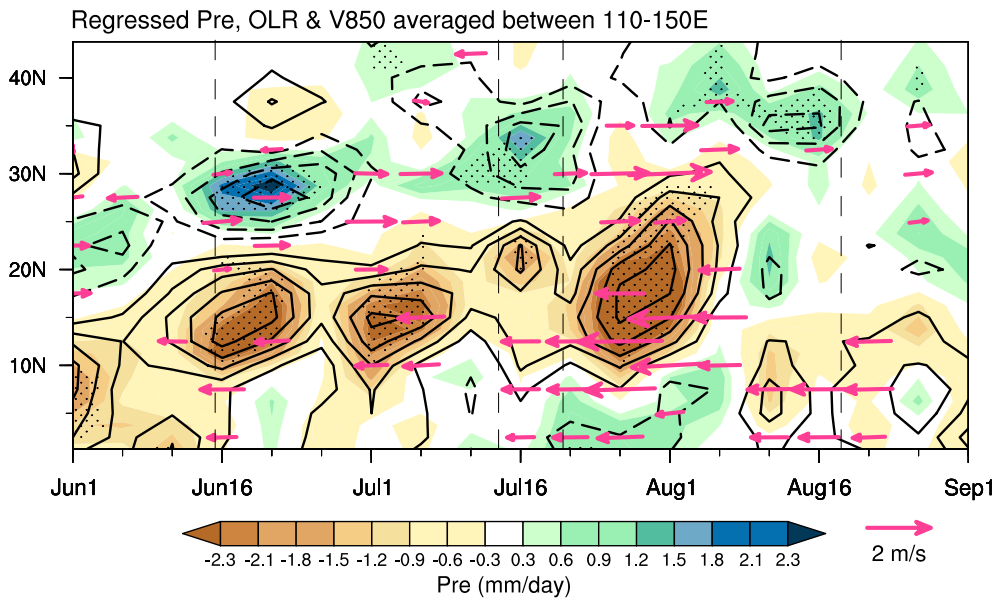
652



654

655 **Figure 1.** (Left) 850 hPa wind (vectors) and SAT (colors) anomalies, (middle)
 656 vertically integrated (from the surface to 200 hPa) moisture fluxes (vectors) and their divergence (colors),
 657 (right) SST anomalies (colors) in (a, b, c) June, (d, e, f) July, (g, h, i) August regressed against
 658 standardized DJF(0) Niño3.4 index for 1978/79–2015/16. Vectors only exceeding the 90%
 659 confidence level are shown and dots indicate that the anomalies are significant at the 90%
 660 confidence level. The hatched areas from west to east (c) indicate NA, NIO and NWP,
 661 respectively.

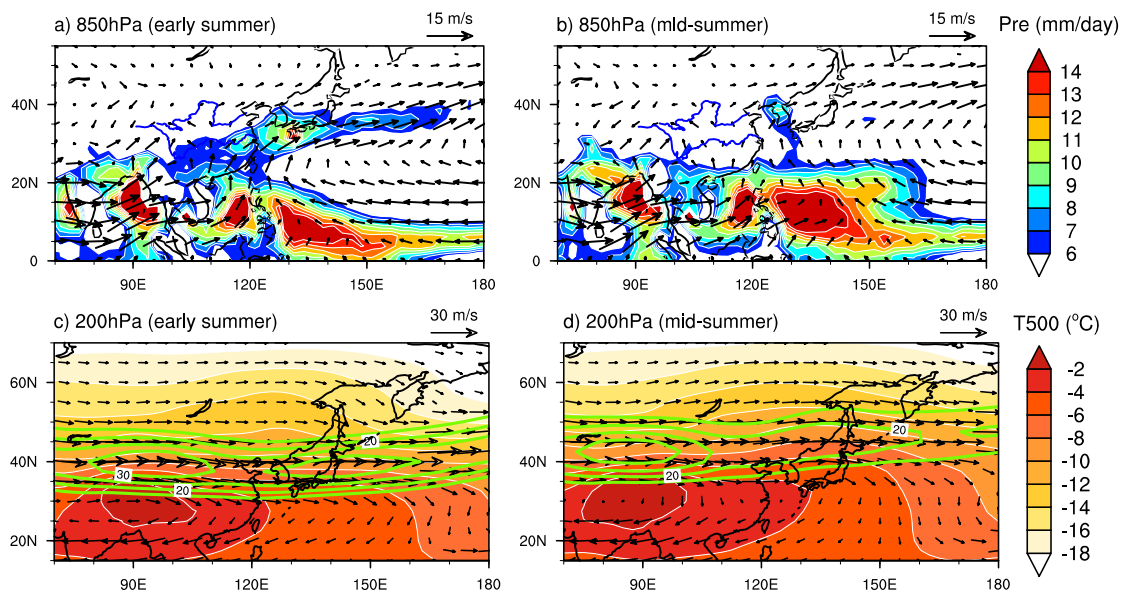
662



663

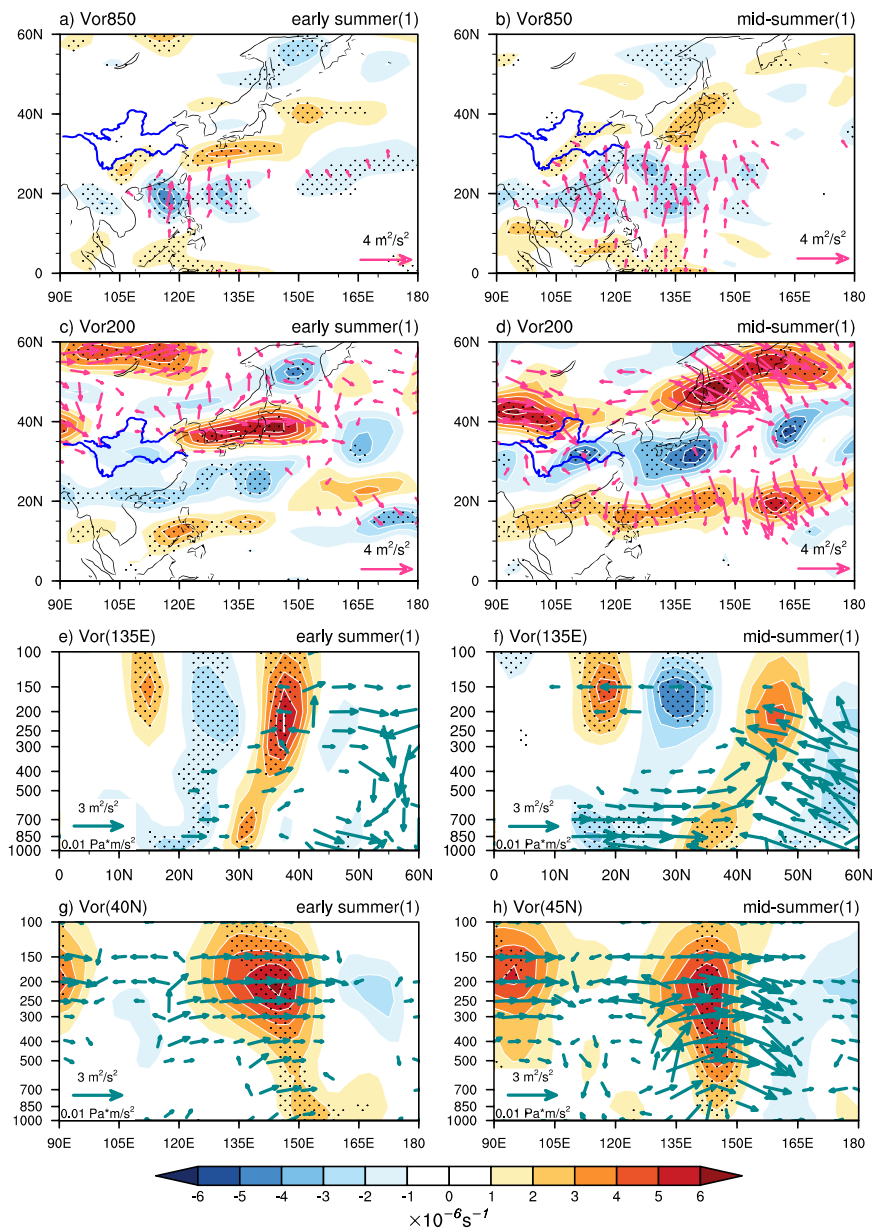
664 **Figure 2.** 850 hPa wind (vectors, shown only exceeding the 90% confidence level),
665 precipitation (colors, dots indicate that the anomalies are significant at the 90% confidence
666 level) and OLR (contours for ± 2 , ± 4 , ± 6 , ± 8) anomalies averaged between 110° - 150° E
667 regressed against standardized DJF(0) Niño3.4 index for 1978/79–2015/16. Solid and dashed
668 contours represent negative and positive convection anomalies, respectively. Early summer(1)
669 is defined as 15 June(1)-14 July(1) and mid-summer(1) 20 July(1)-18 August(1).

670



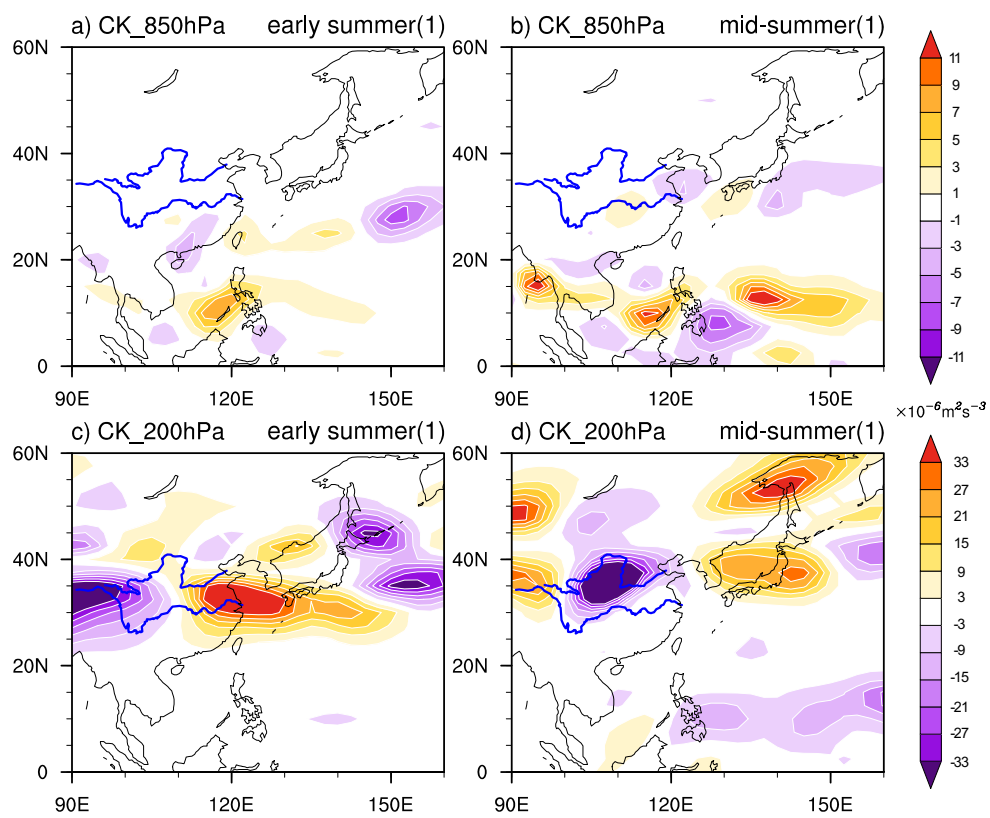
671

672 **Figure 3.** Climatological mean horizontal winds (vectors) at 850 hPa (a, b) and 200 hPa (c, d),
673 superimposed on the climatological mean precipitation (colors; a, b) and air temperature at 500
674 hPa (colors; c, d) in the early and mid- summer. Climatological mean zonal winds are also
675 overlaid (contours for 15, 20, 25, 30 m/s; c, d).



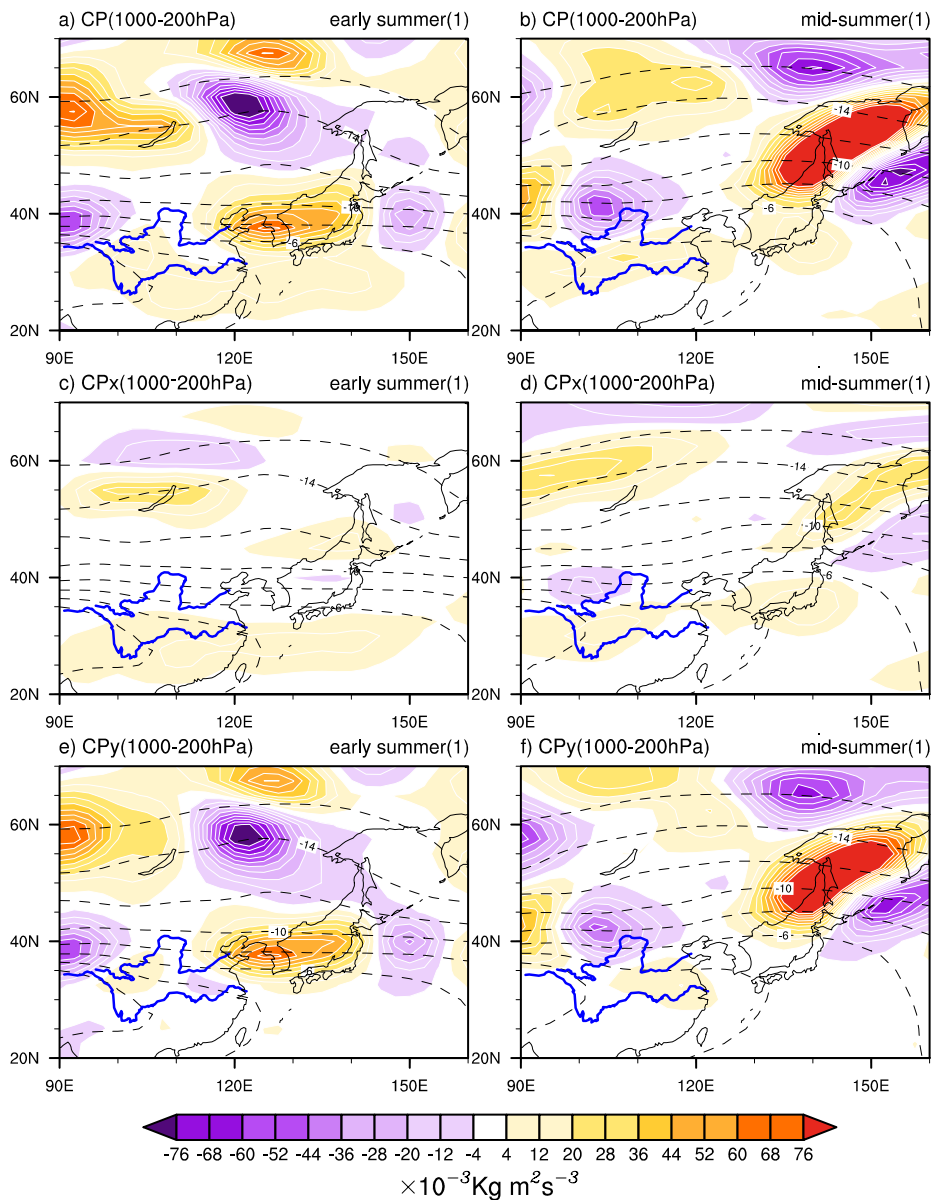
677
 678 **Figure 4.** Relative vorticity anomalies (colors, dots indicate that the anomalies are significant
 679 at the 90% confidence level) at (a, b) 850 hPa and (c, d) 200 hPa in (a, c) early summer, (b, d)
 680 mid-summer regressed against standardized DJF(0) Niño3.4 index for 1978/79–2015/16.
 681 Meridional section of regressed vorticity anomalies (colors) at (e, f) 135°E in the early and
 682 mid-summer(1), respectively. Zonal section of regressed vorticity anomalies (colors) at (g) 40°
 683 and (h) 45°N in the early and mid-summer(1), respectively. Vectors denote the corresponding
 684 wave fluxes.

685



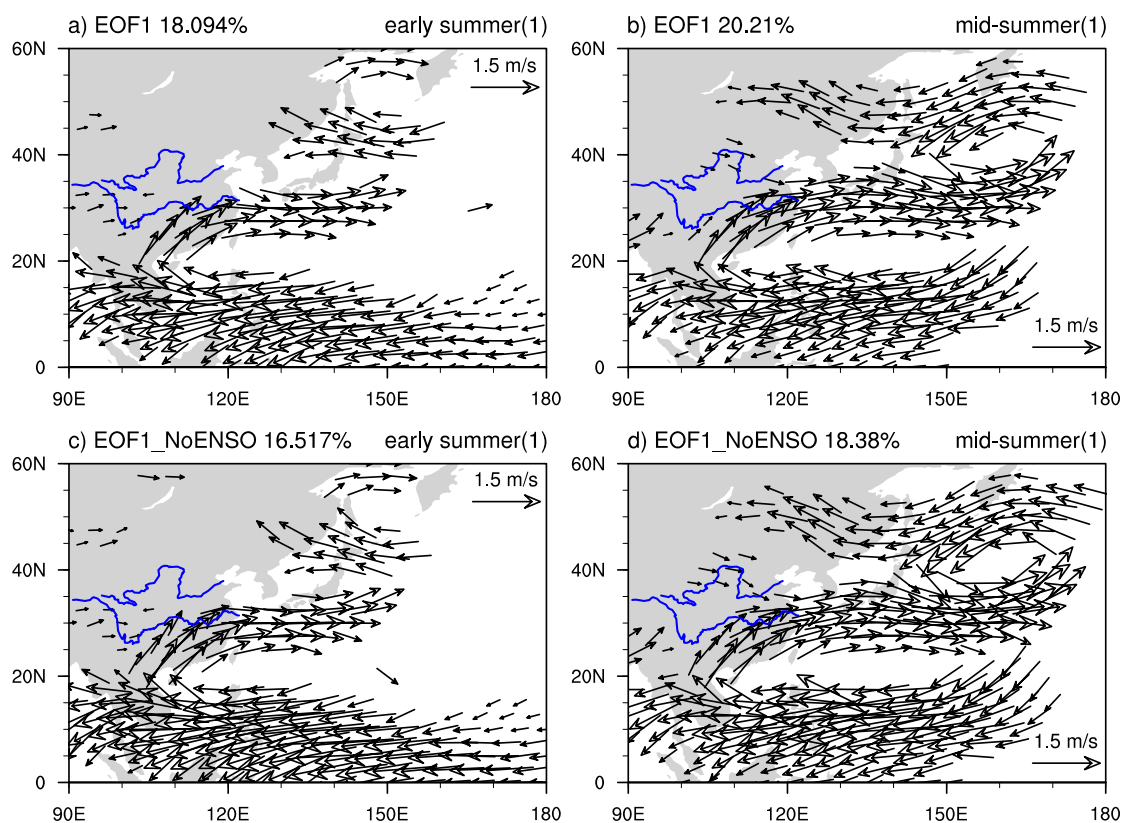
686

687 **Figure 5.** Barotropic energy conversion *CK* at 850 hPa and 200 hPa during El Niño decaying
688 early summer (a, c) and mid-summer (b, d).



690

691 **Figure 6.** Vertically integrated (1000-200 hPa) baroclinic energy conversion CP (colors) and
 692 climatological mean temperature at 500 hPa (contours, °C) during El Niño decaying early
 693 summer (a) and mid-summer (b). Also shown are CP_x and CP_y in the Eq. (2) during El Niño
 694 decaying early summer (c, e) and mid-summer (d, f).



696

697 **Figure 7.** 850 hPa wind anomalies (vectors) regressed against standardized PC1 of the EOF
 698 analyses performed on standardized 850 hPa vorticity anomalies over the EA-NWP (10°-60°N,
 699 100°-160°E) during El Niño decaying early summer (a) and mid-summer (b). c (d) is the same
 700 as a (b) but on the 850 hPa vorticity anomalies independent of ENSO. Vectors only exceeding
 701 the 90% confidence level are shown.

Figures

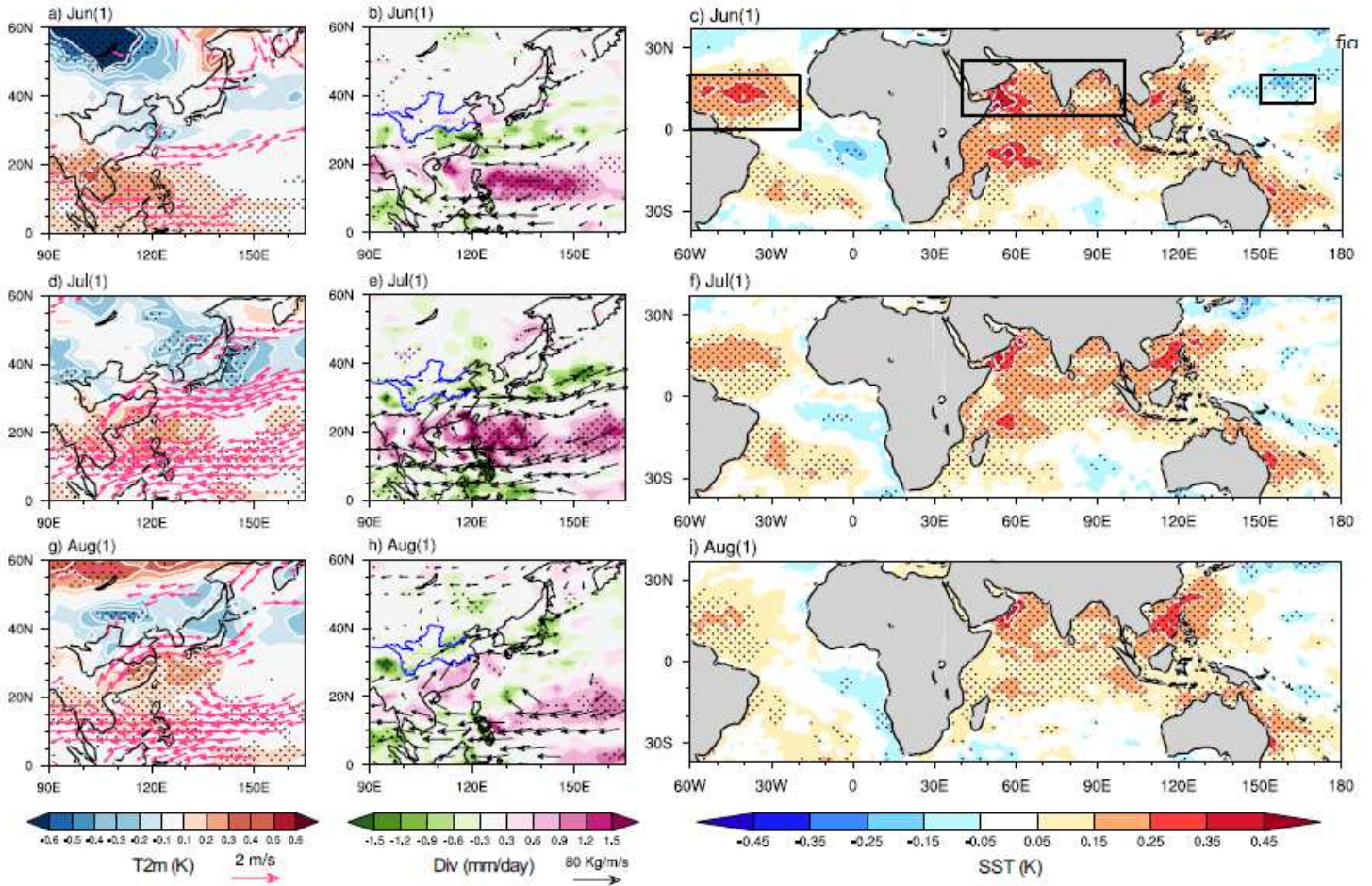


Figure 1

(Left) 850 hPa wind (vectors) and SAT (colors) anomalies, (middle) vertically integrated (from the surface to 200 hPa) moisture fluxes (vectors) and their divergence (colors), (right) SST anomalies in (a, b, c) June, (d, e, f) July, (g, h, i) August regressed against standardized DJF(0) Niño3.4 index for 1978/79–2015/16. Vectors only exceeding the 90% confidence level are shown and dots indicate that the anomalies are significant at the 90% confidence level. The hatched areas from west to east (c) indicate NA, NIO and NWP, respectively. Note: The designations employed and the presentation of the material on this map do not imply the expression of any opinion whatsoever on the part of Research Square concerning the legal status of any country, territory, city or area or of its authorities, or concerning the delimitation of its frontiers or boundaries. This map has been provided by the authors.

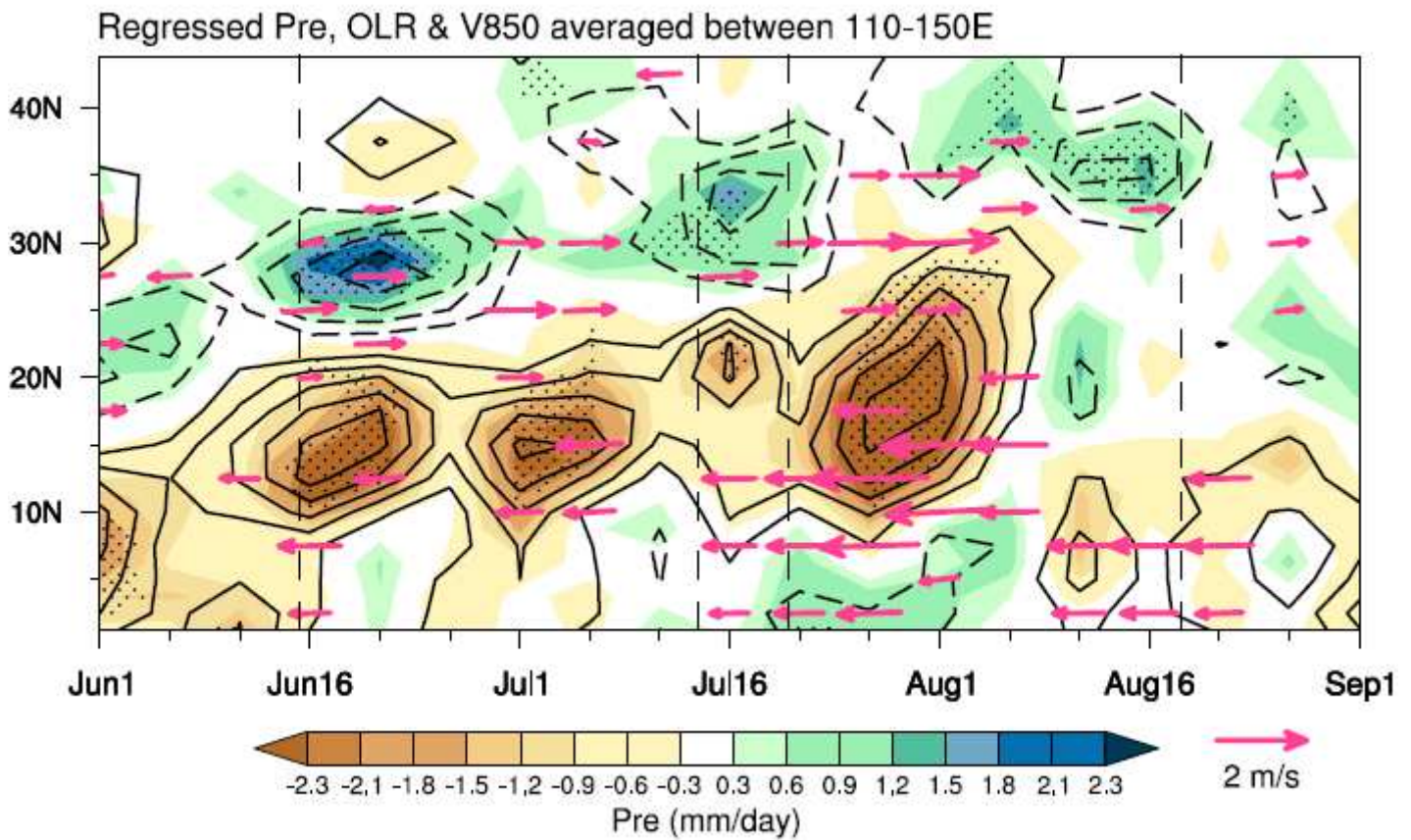


Figure 2

850 hPa wind (vectors, shown only exceeding the 90% confidence level), precipitation (colors, dots indicate that the anomalies are significant at the 90% confidence level) and OLR (contours for ± 2 , ± 4 , ± 6 , ± 8) anomalies averaged between 110°-150°E regressed against standardized DJF(0) Niño3.4 index for 1978/79–2015/16. Solid and dashed contours represent negative and positive convection anomalies, respectively. Early summer(1) is defined as 15 June(1)–14 July(1) and mid-summer(1) 20 July(1)–18 August(1).

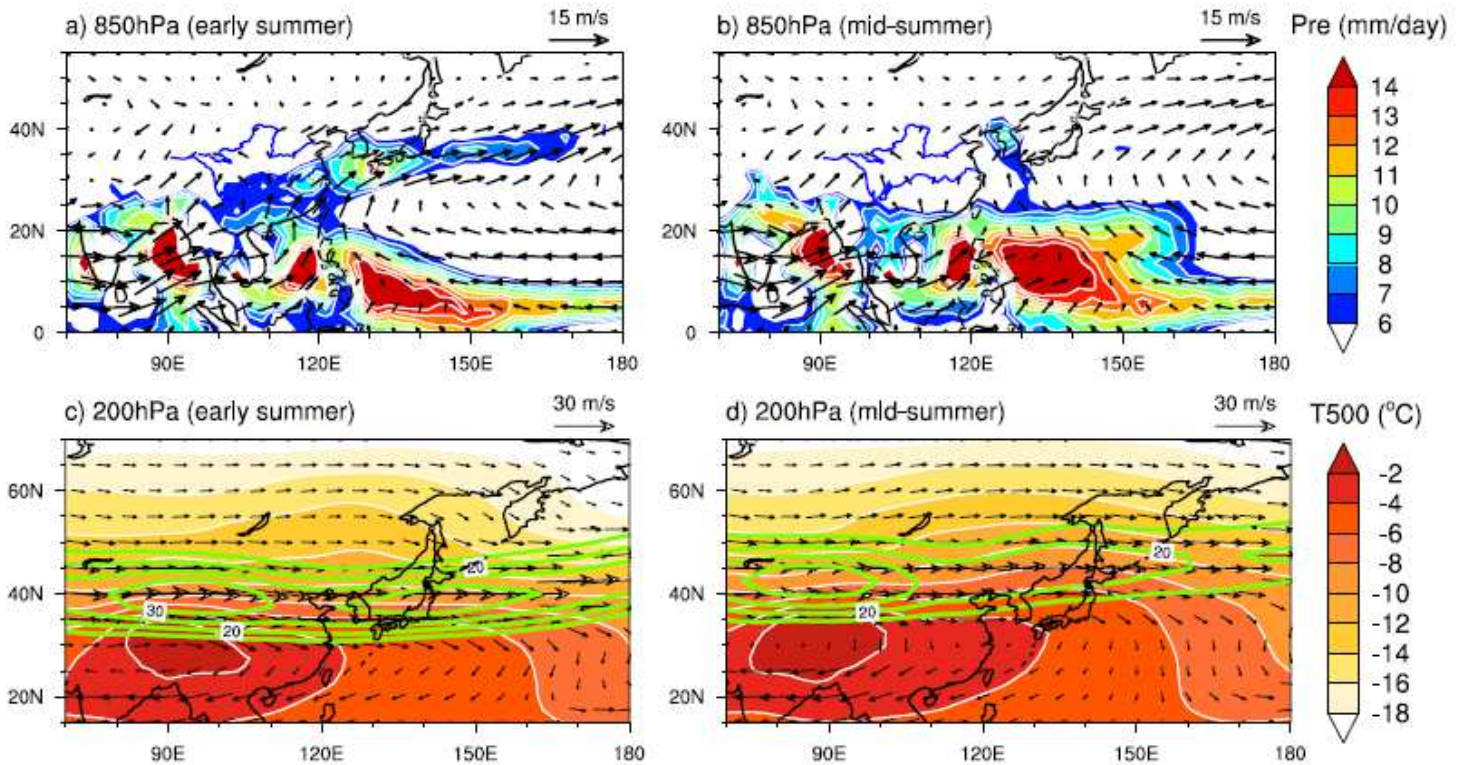


Figure 3

Climatological mean horizontal winds (vectors) at 850 hPa (a, b) and 200 hPa (c, d), superimposed on the climatological mean precipitation (colors; a, b) and air temperature at 500 hPa (colors; c, d) in the early and mid- summer. Climatological mean zonal winds are also overlaid (contours for 15, 20, 25, 30 m/s; c, d). Note: The designations employed and the presentation of the material on this map do not imply the expression of any opinion whatsoever on the part of Research Square concerning the legal status of any country, territory, city or area or of its authorities, or concerning the delimitation of its frontiers or boundaries. This map has been provided by the authors.

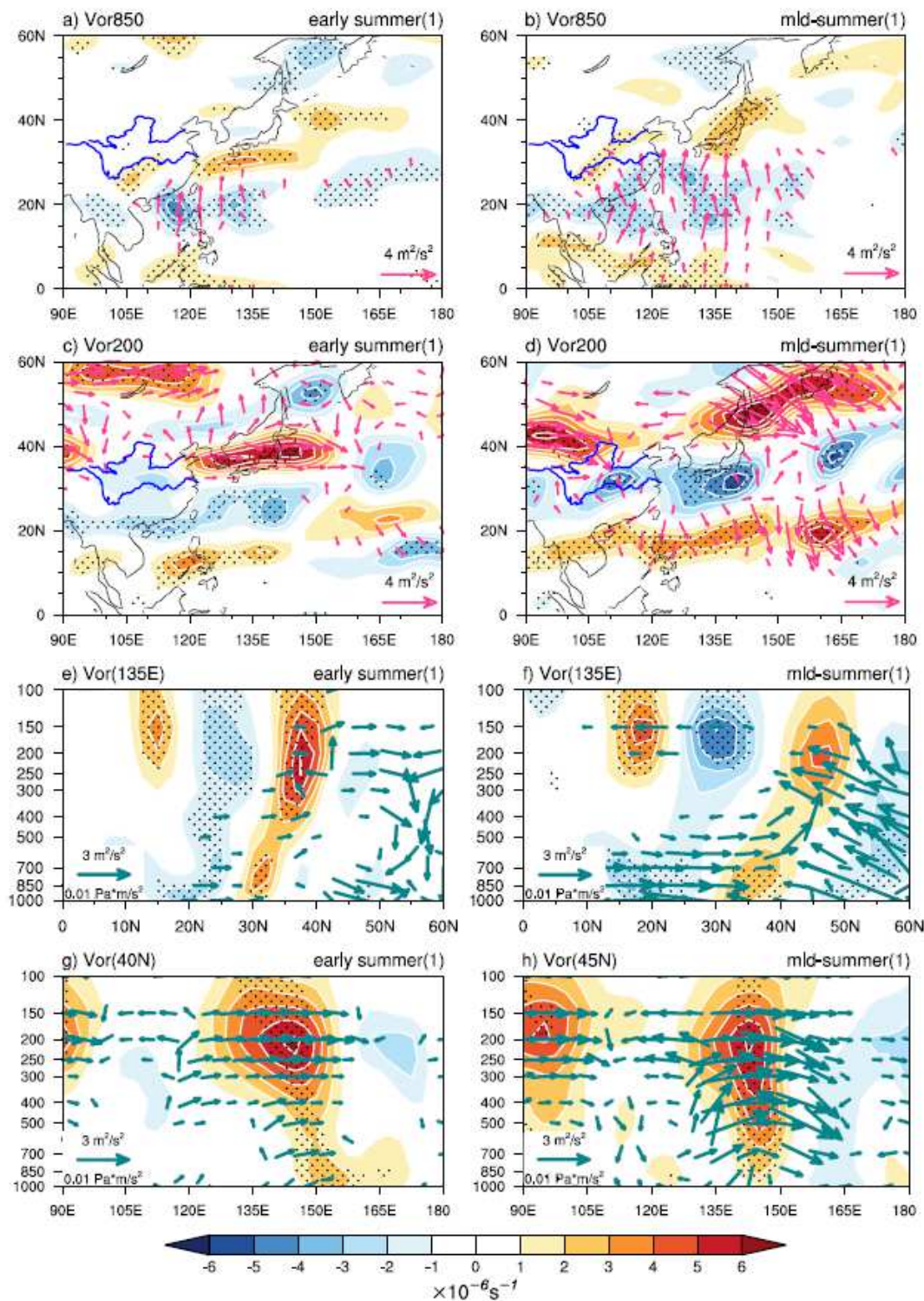


Figure 4

Relative vorticity anomalies (colors, dots indicate that the anomalies are significant at the 90% confidence level) at (a, b) 850 hPa and (c, d) 200 hPa in (a, c) early summer, (b, d) mid-summer regressed against standardized DJF(0) Niño3.4 index for 1978/79–2015/16. Meridional section of regressed vorticity anomalies (colors) at (e, f) 135°E in the early and mid-summer(1), respectively. Zonal section of regressed vorticity anomalies (colors) at (g) 40° and (h) 45°N in the early and mid-summer(1),

respectively. Vectors denote the corresponding wave fluxes. Note: The designations employed and the presentation of the material on this map do not imply the expression of any opinion whatsoever on the part of Research Square concerning the legal status of any country, territory, city or area or of its authorities, or concerning the delimitation of its frontiers or boundaries. This map has been provided by the authors.

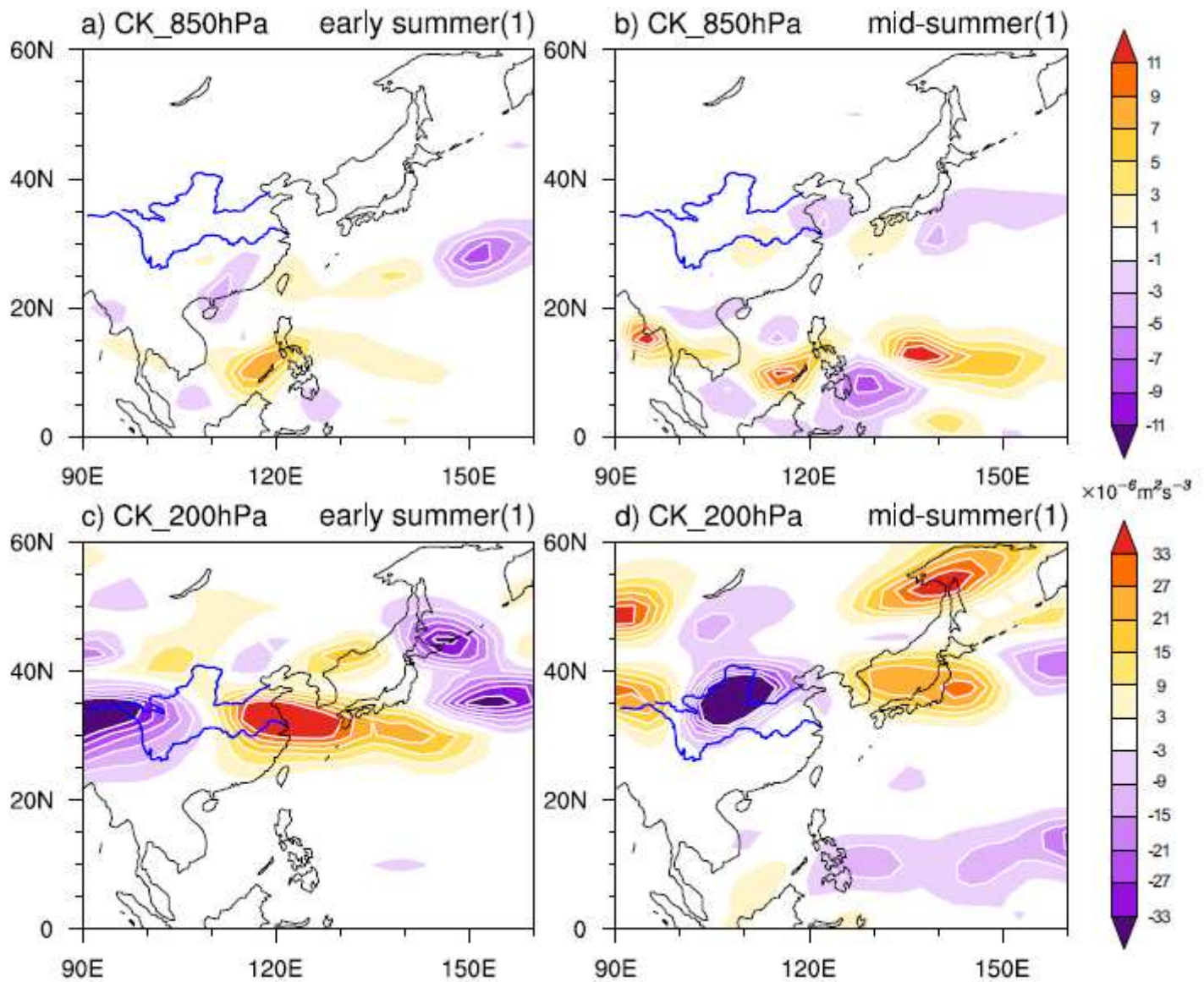


Figure 5

Barotropic energy conversion CK at 850 hPa and 200 hPa during El Niño decaying early summer (a, c) and mid-summer (b, d). Note: The designations employed and the presentation of the material on this map do not imply the expression of any opinion whatsoever on the part of Research Square concerning the legal status of any country, territory, city or area or of its authorities, or concerning the delimitation of its frontiers or boundaries. This map has been provided by the authors.

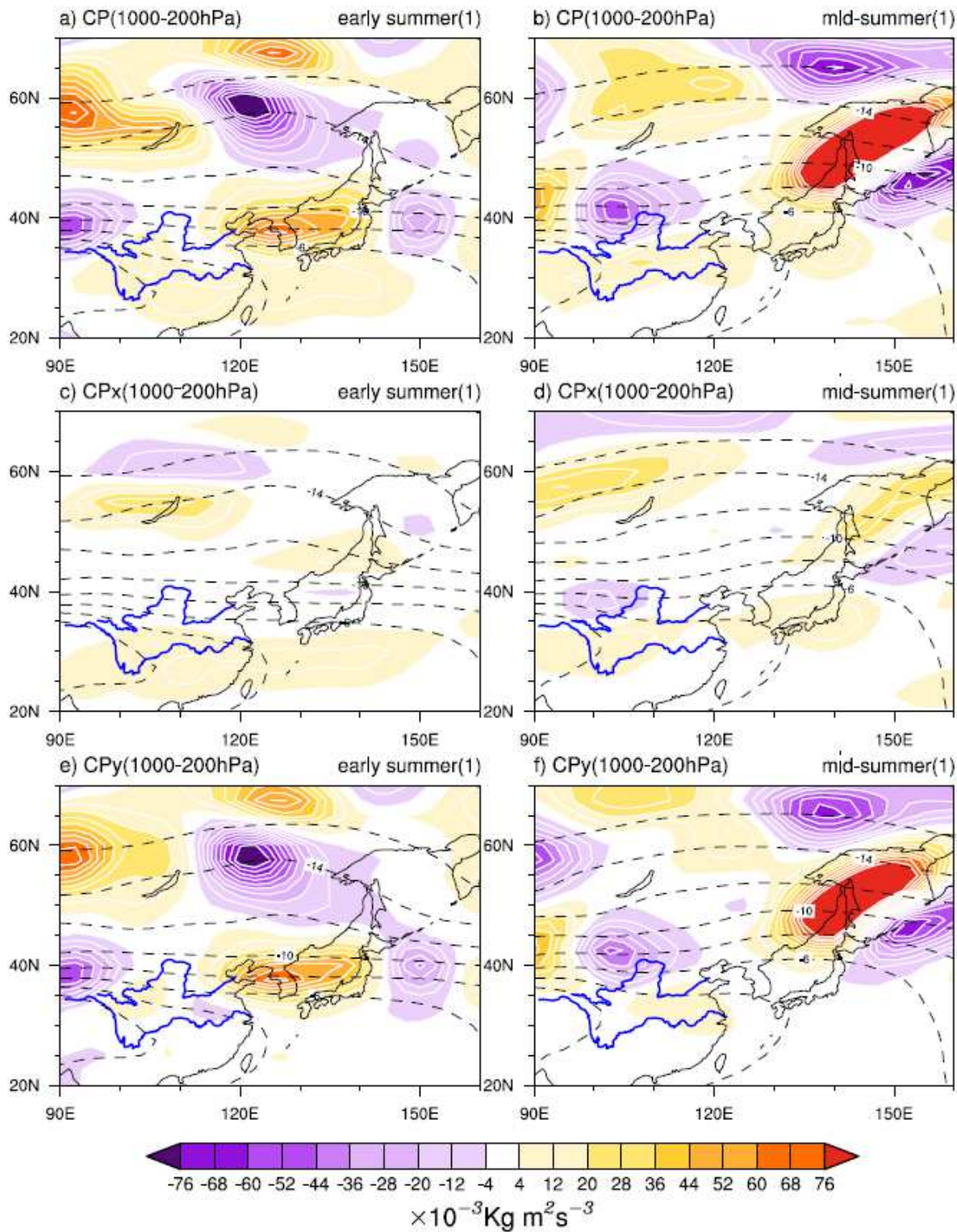


Figure 6

Vertically integrated (1000-200 hPa) baroclinic energy conversion CP (colors) and climatological mean temperature at 500 hPa (contours, °C) during El Niño decaying early summer (a) and mid-summer (b). Also shown are \overline{u} and \overline{v} in the Eq. (2) during El Niño decaying early summer (c, e) and mid-summer (d, f). Note: The designations employed and the presentation of the material on this map do not imply the expression of any opinion whatsoever on the part of Research Square concerning the legal status of any

country, territory, city or area or of its authorities, or concerning the delimitation of its frontiers or boundaries. This map has been provided by the authors.

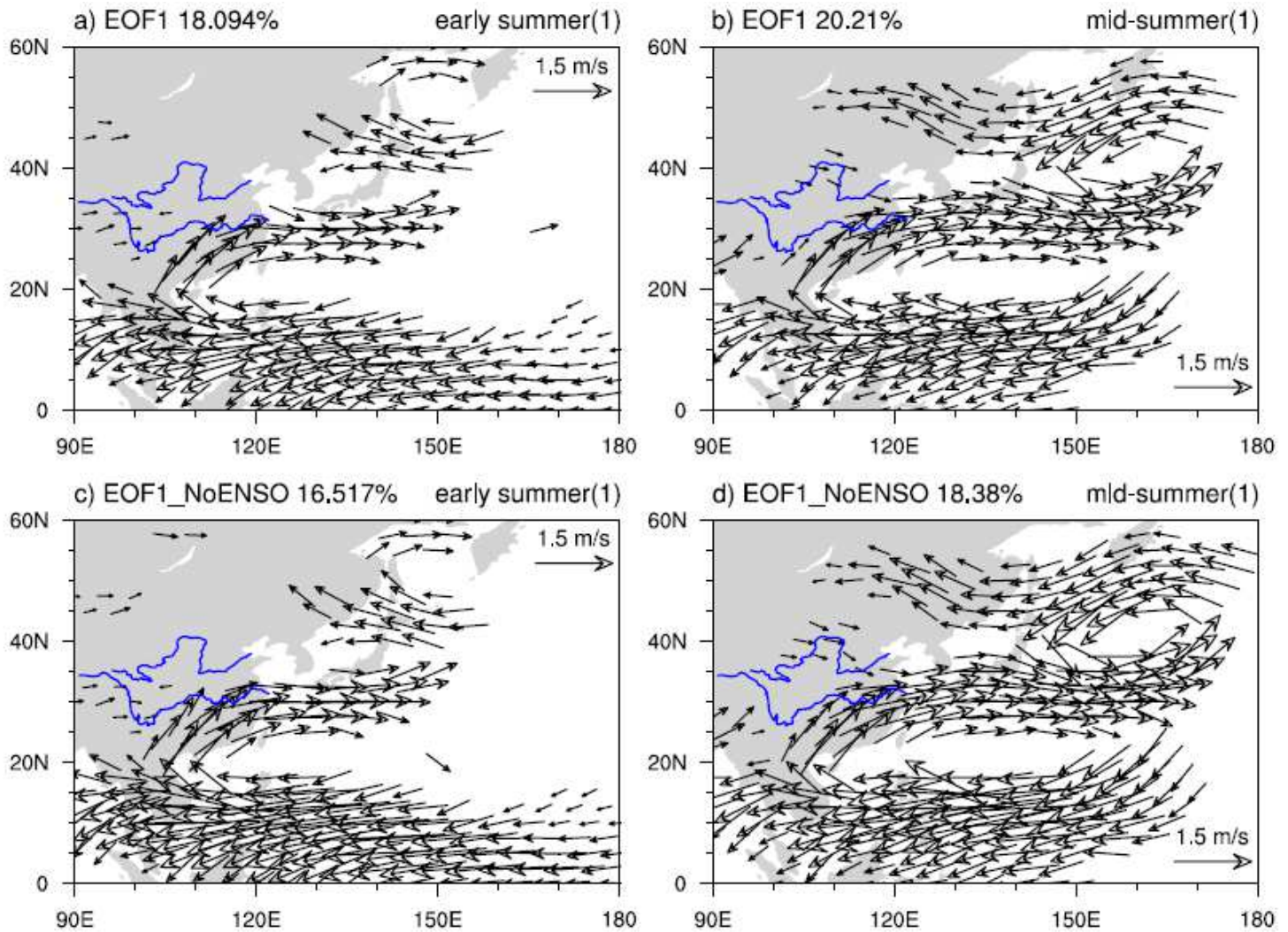


Figure 7

850 hPa wind anomalies (vectors) regressed against standardized PC1 of the EOF analyses performed on standardized 850 hPa vorticity anomalies over the EA-NWP (10°-60°N, 100°-160°E) during El Niño decaying early summer (a) and mid-summer (b). c (d) is the same as a (b) but on the 850 hPa vorticity anomalies independent of ENSO. Vectors only exceeding the 90% confidence level are shown. Note: The designations employed and the presentation of the material on this map do not imply the expression of any opinion whatsoever on the part of Research Square concerning the legal status of any country, territory, city or area or of its authorities, or concerning the delimitation of its frontiers or boundaries. This map has been provided by the authors.